Atmos. Meas. Tech., 8, 4539–4559, 2015
www.atmos-meas-tech.net/8/4539/2015/
doi:10.5194/amt-8-4539-2015

Atmospheric Measurement Techniques
Open Access
EGU

Local- and regional-scale measurements of CH_4, $\delta^{13}CH_4$, and C_2H_6 in the Uintah Basin using a mobile stable isotope analyzer

C. W. Rella, J. Hoffnagle, Y. He, and S. Tajima

Picarro, Inc., 3105 Patrick Henry Drive, Santa Clara 95054, CA, USA

Correspondence to: C. W. Rella (rella@picarro.com)

Received: 19 February 2015 – Published in Atmos. Meas. Tech. Discuss.: 13 May 2015
Revised: 28 September 2015 – Accepted: 4 October 2015 – Published: 30 October 2015

Abstract. In this paper, we present an innovative CH_4, $\delta^{13}CH_4$, and C_2H_6 instrument based on cavity ring-down spectroscopy (CRDS). The design and performance of the analyzer is presented in detail. The instrument is capable of precision of less than 1 ‰ on $\delta^{13}CH_4$ with 1 in. of averaging and about 0.1 ‰ in an hour. Using this instrument, we present a comprehensive approach to atmospheric methane emissions attribution. Field measurements were performed in the Uintah Basin (Utah, USA) in the winter of 2013, using a mobile lab equipped with the CRDS analyzer, a high-accuracy GPS, a sonic anemometer, and an onboard gas storage and playback system. With a small population and almost no other sources of methane and ethane other than oil and gas extraction activities, the Uintah Basin represents an ideal location to investigate and validate new measurement methods of atmospheric methane and ethane. We present the results of measurements of the individual fugitive emissions from 23 natural gas wells and six oil wells in the region. The $\delta^{13}CH_4$ and C_2H_6 signatures that we observe are consistent with the signatures of the gases found in the wells. Furthermore, regional measurements of the atmospheric CH_4, $\delta^{13}CH_4$, and C_2H_6 signatures throughout the basin have been made, using continuous sampling into a 450 m long tube and laboratory reanalysis with the CRDS instrument. These measurements suggest that 85 ± 7 % of the total emissions in the basin are from natural gas production.

1 Introduction

The advent of the techniques of directional drilling, horizontal drilling, 3-D seismic imaging, and hydraulic fracturing have led to rapid increases in oil and gas production throughout the US, especially in basins where production using so-called conventional methods of extraction was not economically viable. Together with the increase of oil and gas production, there has been a concurrent increase in gaseous emissions into the atmosphere. Methane, the primary constituent of natural gas, is a potent greenhouse gas with a global warming potential of up to 86 times that of an equivalent mass of carbon dioxide over a 20-year timescale. With a moderate atmospheric lifetime of 12.4 years, the relative impact of methane on a 100-year timescale is 28 (Myhre et al., 2013). When emissions are kept under control, methane is a clean-burning, high energy content fuel that can reduce carbon dioxide emissions relative to other more carbon-rich fuels. However, when methane emissions are a relatively large fraction of total natural gas production, the climate benefit of natural gas relative to coal (a relatively carbon-intensive fuel) is reduced or even eliminated (Alvarez et al., 2012).

Several recent atmospheric studies using the aircraft mass-balance approach have focused on quantifying regional emissions from oil and gas production. In Pétron et al. (2014), the mass-balance approach using aircraft was used to quantify emissions in the Denver–Julesburg Basin in Colorado, determining that the methane emissions from fossil fuel extraction activities are about 4 % of total natural gas production in the basin. This emission rate is in excess of both the inventory (Pétron et al., 2012) and the ~ 3 % threshold where there are immediate climate benefits of switching from coal to natural gas electricity production (Alvarez et al., 2012). In the Uintah Basin in Utah, again using aircraft, Karion et al. (2013) reported methane emissions (February, 2012) to be 6.2–11.7 % of average daily production from the basin, again exceeding the inventory and the threshold for immediate climate bene-

fit. Other studies using this approach are underway in several other basins in the US.

Top-down measurements of regional emissions provide crucial independent verification of bottom-up emission inventories. However, the mass-balance measurements of total methane emissions do not provide a means of partitioning the emissions i.e., determining the relative fraction of emissions contributed by the source types within the aircraft footprint. While the Uintah Basin is fairly simple from the standpoint of methane emissions, with a small population ($\sim 60\,000$) and no significant sources of methane apart from oil and gas extraction, the oil- and gas-producing area in the Denver–Julesburg Basin is largely co-located with other sources of methane, such as landfills and concentrated animal feeding operations. Pétron et al. (2014) estimate these emissions to be about 25–30 % of the total on the basis of emission inventories for other sources, such as enteric fermentation, manure management, and solid waste disposal, but without an independent measurement of this inventory, the uncertainty of the emissions attributed to oil and gas activities remains high.

Tracer molecules (i.e., molecules that are co-emitted with methane in different ratios depending upon the emissions sector) can provide valuable information to partition regional emissions. In particular, the stable isotopes of methane and alkanes (ethane, propane, etc.) have been shown to be valuable in partitioning methane emissions between various sources (Dlugokencky et al., 2011). It has long been understood that low ethane to methane ratios ($\ll 1\,\%$) and light $\delta^{13}CH_4$ signatures below $-64\,‰$ indicate a purely biogenic (i.e., microbial) source (Schoell, 1980). Quay et al. (1988) compile $\delta^{13}CH_4$ signatures from a variety of microbial and abiogenic sources.

The use of the atmospheric signals of $\delta^{13}CH_4$ and ethane to infer methane sources and sinks is a relatively new and active area of research. On a global scale, atmospheric measurements of $\delta^{13}CH_4$ have been used to partition emissions of methane (Mikaloff-Fletcher et al., 2004a, b). Atmospheric measurements of methane and of $\delta^{13}CH_4$ since 1990 have been used to infer changes in the balance between biogenic and thermogenic sources of methane (Kai et al., 2011). In Lowry et al. (2001), the diurnal signal of CH_4 and $\delta^{13}CH_4$ in the vicinity of London was used to partition emissions between biogenic sources (in this case, landfills and waste treatment) and the natural gas distribution system. Isotopic methane measurements were employed to infer methane sources in arctic air masses (Fisher et al., 2011). Isotopic measurements have also been used to perform source partitioning over time, by analyzing firn air (Bräunlich et al., 2001; Mischler et al., 2009). Ethane has been used in a similar manner globally. For example, Simpson et al. (2012) demonstrated a strong correlation between global ethane concentration and the global methane growth rate to suggest that the overall decrease in the global growth rate of methane over the past 30 years is due to a decrease in oil and gas emissions, although these findings are not fully consistent with other studies (for example, Kirschke et al., 2013) that show tropical wetlands emissions of methane also play an important role. What is clear is that more measurements of these important atmospheric tracers can provide useful constraints on global methane sources and sinks.

These tracers have also been used to infer attribution of emissions on a regional scale. $\delta^{13}CH_4$ was used to suggest a relative increase in methane emissions from biogenic sources in Germany from 1992 to 1996 (Levin et al., 1999). Smith et al. (2000) used $\delta^{13}CH_4$ and δCH_3D to identify emissions mechanisms in the Orinoco river flood plain in Venezuela. In Xiao et al. (2008), atmospheric measurements of ethane were used to constrain oil and gas emissions in the US.

Despite their clear utility, $\delta^{13}CH_4$ and ethane measurements have not enjoyed more widespread use, primarily due to the lack of easy-to-use instrumentation capable of accurate real-time measurements in the field. Traditionally, stable isotope analysis has been the domain of chromatographic separation of methane followed by continuous flow isotope ratio mass spectrometry (GC-CF-IRMS). Isotope ratio precision of 0.05 ‰ has been achieved with this type of system (Fisher et al., 2006). In this paper, we present a new approach to emissions attribution, using a CH_4, $\delta^{13}CH_4$, and C_2H_6 instrument based on cavity ring-down spectroscopy (CRDS). CRDS is an analytical technique in which the infrared absorption of a gas sample is measured by quantifying the optical decay rate of a highly resonant optical cell into which the gas sample is introduced. This easy-to-use, field-deployable instrument is capable of simultaneous measurements of methane with < 1 ppb typical precision (1-σ) in < 5 s, $\delta^{13}CH_4$ with 1 ‰ typical precision in 1 min and about 0.1 ‰ in an hour, and C_2H_6 with about 20 ppb typical precision in 1 min and less than 10 ppb in 1 h. Typical concentrations of methane and ethane in the clean continental atmosphere are 1.7–1.9 ppm and 0.5–2.0 ppb, respectively, but in regions where emissions of these gases are high, concentrations can rise as high as ~ 10 ppm CH_4 and ~ 1000 ppb C_2H_6. At these levels, this instrument is useful for individual source characterization as well as quantification of the overall atmospheric signature in a given region, activities that are crucial to regional source apportionment.

Using a mobile lab equipped with the CRDS analyzer, a high-accuracy GPS, a sonic anemometer, and an onboard gas storage and playback system, field measurements were performed in the Uintah Basin (Utah, USA) in the winter of 2013. The Uintah Basin has about 5000 active gas wells and 3000 active oil wells in the basin (Utah Well Information Query, 2012). Since 2000, gas production has increased from 100 BCFE yr^{-1} (billion cubic feet based on a constant energy content metric; 1 BCF $= 2.83 \times 10^7$ m^3) to more than 300 BCFE yr^{-1} in 2013 (UBETS Report, 2013). Over the same time period, oil production has increased from 8 MMBOE yr^{-1} (million barrels of oil based on a constant energy metric; one barrel = 159 L) to nearly 20 MMBOE yr^{-1}, along with a fourfold increase in natu-

ral gas liquids (UBETS Report, 2013). In addition to the high methane emissions deduced from aircraft measurements (Karion et al., 2013), the Uintah Basin suffers from poor air quality due to high production of ozone in the wintertime during atmospheric inversion events. Studies have shown that the gaseous effluents of oil and gas extraction activities in the basin are a key ingredient for the high ozone production (Edwards et al., 2013; Schnell et al., 2012). Although it is clear that the vast majority of methane emissions originate from oil and gas activities (primarily extraction and processing), the relative proportions of emissions associated with the oil production sector and the gas production sector have not been well understood, until now: the mobile CH_4, $\delta^{13}CH_4$, and C_2H_6 analysis described in this paper indicates that the emissions from natural gas production comprise 85 ± 7 % (1-σ) of the emissions in the basin, with the remainder from oil production activities and biogenic sources.

The paper is organized as follows: we first present a detailed description of the CRDS analyzer used in this study, including a thorough discussion of performance, calibration, and cross-interference from other atmospheric constituents. We then describe the mobile laboratory used to perform the measurements, and the methodology employed for characterization of individual sources and regional signals. Results for individual source measurements are presented and compared to studies of the gas composition present in the geologic formations in gas- and oil-producing areas of the basin. These individual source signatures are then used to interpret the regional atmospheric signal using a simple two-end-member model. We conclude the paper with a discussion of the findings and present a future outlook for the measurement technology presented.

2 Instrument performance

2.1 Details of the cavity ring-down spectrometer

The methane and ethane measurements were made with an optical analyzer based on cavity ring-down spectroscopy (G2132-*i*, S/N FCDS2016, Picarro, Inc., Santa Clara, CA). CRDS is a laser-based technique in which the infrared absorption loss in a sample cell is measured to quantify the mole-fraction of the gas or gases. Five gas species are measured by this instrument: $^{12}C^{1}H_4$, $^{13}C^{1}H_4$, $^{1}H_2^{16}O$, $^{12}C_2^{1}H_6$, and $^{12}C^{16}O_2$ (the latter three are denoted H_2O, C_2H_6, and CO_2 from here onward).

CRDS is a method in which laser light is coupled into a resonant optical cell. The decay rate of the optical power in the cavity is a direct measurement of the total loss, which includes both absorption loss due to the gas mixture contained in the optical cell and the loss of the mirrors in the system. Two separate lasers are used in this spectrometer: one for the $^{12}CH_4$ and CO_2 measurements operating at about 6057 wavenumbers, and one for the $^{13}CH_4$, H_2O, and C_2H_6 measurements operating at about 6029 wavenumbers. Light from each laser, tuned to specific near-infrared absorption features of the key analyte molecules, is directed sequentially into an optical resonator (called the optical cavity). The optical cavity consists of a closed chamber with three highly reflective mirrors, and it serves as a compact flow cell with a volume of less than 10 standard cm^3 into which the sample gas is introduced. The sample gas is flowed continuously through the system. The gas flow in the standard instrument is about 25 sccm, but by either modifying the inlet plumbing system and/or restricting the inlet flow, the instrument can be operated at flows from 5 to 400 sccm. The measurements described in this paper were taken at 400 sccm in the mobile laboratory, for fast response ($\sim$ 1 s 10–90 % rise/fall time); and at 15–20 sccm for laboratory work, for conservation of sample gas. The optical cavity is actively controlled to a temperature of 45 °C, and the gas in the cell is actively controlled to a pressure of 148 Torr.

The flow cell has an effective optical path length of 15–20 km; this long path length allows for measurements with high precision (with ppb or even parts per trillion uncertainty, depending on the analyte gas), using compact and highly reliable near-infrared laser sources. The gas temperature and pressure are tightly controlled in these instruments (Crosson, 2008). This stability allows the instrument (when properly calibrated to traceable reference standards) to deliver accurate measurements (Richardson et al., 2012).

The instrument employs precise monitoring and control of the optical wavelength, which delivers sub-picometer wavelength targeting on a microsecond timescale. When the laser is at the proper wavelength and is in resonance with the optical cell, the laser is turned off. The resulting decay of optical power, called a ring-down, is measured with a fast photodetector. From the ring-down decay time the total absorbance of the system is derived using the equation $\alpha = \frac{1}{c\tau}$, where α is the absorbance, τ is the ring-down time, and c is the speed of light. Ring-down events are collected at a rate of about 200 ring-downs s^{-1}. Individual spectrograms consist of about 50–200 individual ring-downs, distributed across 10–20 spectral points around the peak. The overall measurement interval is about 1 s. The resulting spectrograms are analyzed using nonlinear spectral pattern recognition routines, and the outputs of these routines are converted into gas concentrations using linear conversion factors derived from calibration activities using gas standards that are traceable to gravimetric standards or other artifact standards, as described below.

2.2 $^{12}CH_4$ and $^{13}CH_4$ spectroscopy

The right panel of Fig. 1 displays the spectra of key gas species, which includes the five analytical species and other atmospheric constituents that absorb in the 6057 wavenumber region, generated with the HITRAN database (Rothman et al., 2013) for CH_4, CO_2, and H_2O. The spectral feature

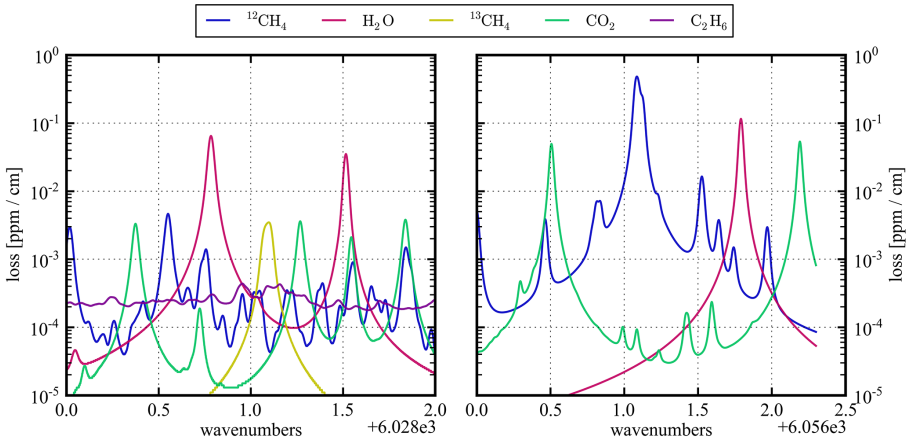

Figure 1. Spectra of key species in the frequency ranges employed in the spectrometer, displaying loss on a log scale vs. optical frequency in wavenumbers for the low-frequency region (left panel) and high-frequency region (right panel). The spectra for methane (both isotopologues, concentration of 2 ppm), water vapor (1 %), and carbon dioxide (400 ppm) are obtained from the HITRAN spectral database (Rothman et al., 2013), for a pressure of 148 Torr and $T = 45\,^{\circ}C$. The ethane spectrum (for a concentration of 1 ppm) was obtained experimentally using CRDS from a 400 ppm bottle.

used for quantification of $^{12}CH_4$ is a quartet of lines centered at about 6057.07 wavenumbers. The laser is scanned across this spectral feature, from about 6056.81 to 6057.39 with approximately 0.02 wavenumber resolution. The resulting spectrograms are fit with a modified nonlinear Levenberg–Marquardt (Press et al., 1986) algorithm, using an experimentally derived model function for $^{12}CH_4$. Due to the complexity of the spectrum, instead of modeling the observed spectrum with an ensemble of single rovibrational transitions, we have constructed an empirically derived model based on a cubic spline with knots spaced approximately every 0.01 wavenumbers.

We note that the spectral region and the analysis algorithms for $^{12}CH_4$ are identical to the algorithms that are used in several standard models from the same manufacturer (e.g., models G1301, G2301, G2401); the performance of these instruments for atmospheric measurements of CH_4, and H_2O has been described in detail elsewhere (Crosson, 2008; Chen et al., 2010; Rella et al., 2013, Fang et al., 2013; Winderlich et al., 2010). The basic performance reported in these papers should be highly representative of the performance of this analyzer, and we will rely on these references for estimates of precision, uncertainty, and crosstalk with key analytical species.

The left panel of Fig. 1 displays the spectra of key gas species (the analytes and other key atmospheric constituents) in the 6029 wavenumber region. The individual spectra were generated from the HITRAN database (Rothman et al., 2013) for CH_4, CO_2, and H_2O, and from experimental measurements for ethane, which is not included in the database. During normal instrument operation, the region of 6028.4–6029.2 wavenumbers is scanned with approximately 0.02 wavenumber resolution. The resulting spectrograms are fit, using experimentally determined model functions for $^{12}CH_4$, $^{13}CH_4$, H_2O, and CO_2. The latter two spectra are quite simple, and were modeled with Galatry functions.

The $^{12}CH_4$ and $^{13}CH_4$ spectra are more complicated to model. Using a prototype instrument, high-resolution spectra over a range of 6028.4–6029.2 wavenumbers were collected on a sample of 100 ppm CH_4 and $\delta^{13}CH_4 \sim -40$ ‰ in a balance of synthetic air. A separate sample of > 99 % pure $^{13}CH_4$ was used to verify that the three lines at 6029.1 are the only significant $^{13}CH_4$ features in this region. All the other lines are due to $^{12}CH_4$. The $^{13}CH_4$ triplet is modeled with Galatry functions (Varghese and Hanson, 1984). The contribution of the $^{13}CH_4$ lines was subtracted from the experimental composite CH_4 spectrum, leaving only $^{12}CH_4$. The $^{12}CH_4$ spectrum was then modeled from this processed spectrum, using a combination of three Galatry functions for the prominent $^{12}CH_4$ peaks and a cubic spline with knots spaced approximately every 0.01 wavenumbers for the smaller peaks. It is possible that the removal of the $^{13}CH_4$ spectrum is imperfect, leading to a cross-interference between $^{12}CH_4$ and $^{13}CH_4$. This cross-interference can be dealt with in a straightforward manner during the calibration of $\delta^{13}CH_4$, as discussed below.

The amplitudes of the $^{12}CH_4$, $^{13}CH_4$, and H_2O spectral features are varied dynamically in the nonlinear fit routine to minimize the least squares. The amplitude of the CO_2 is determined from a quasi-simultaneous measurement of CO_2 made at 6056.51 wavenumbers. CO_2 is measured by scanning from 6056.4 to 6056.6 wavenumbers, across the $^{12}CO_2$ spectral feature. This measurement is only a rough measurement by atmospheric standards ($\sim$ 1 ppm uncertainty), but it is sufficient for the purpose of presetting the strength of the CO_2 lines in the vicinity of the $^{13}CH_4$ feature.

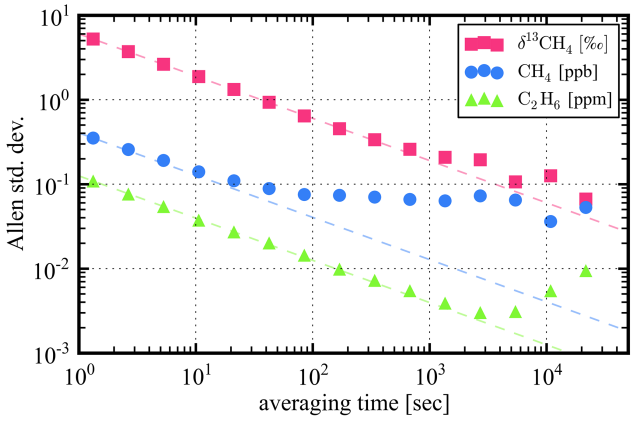

Figure 2. Allan deviation for $\delta^{13}CH_4$, CH_4, and C_2H_6 collected over 18 h, in units of ‰, ppb, and ppm, as noted in the legend. The precision of the instrument is about 0.4 ppb for CH_4 in a 1.2 s measurement, and below 1.0 ‰ for $\delta^{13}CH_4$ in a minute of averaging. The ethane measurement precision is about 20 ppb in 1 min. The latter two quantities follow a square root averaging law for 1 h or more of averaging.

From this nonlinear fit, the water concentration is also determined using the peak height of the water feature centered at 6028.79 wavenumbers. In addition, a second independent nonlinear fit is performed in which the model function of C_2H_6 is also included in the fit, which allows us to quantify the ethane concentration in a gas sample with approximately 100 ppb precision. This relatively poor precision, coupled with an uncorrected cross-interference with some key gas species, limits the general utility of this measurement. The performance and limitations of this measurement are discussed below.

There are two modes of operation in this instrument. In one mode, called the "high-precision" mode, the $^{12}CH_4$ is quantified using the very strong feature at about 6057.07 wavenumbers. In the second mode, called the "high-range" mode, the $^{12}CH_4$ is quantified using the weaker feature at 6028.55 wavenumbers. This line affords the instrument a much larger dynamic range, above 1000 ppm CH_4. In this paper, we consider only the "high-precision" mode of the analyzer. In addition, we will devote most of our attention to the performance of $^{12}CH_4$ and $^{13}CH_4$ (and thus $\delta^{13}CH_4$), since these are the primary analyte gas species. We will also discuss the calibration and uncertainty in the H_2O, CO_2, and C_2H_6 measurements, especially in the context of using these measurements to correct for cross-interference of these species onto the primary analyte gases.

2.3 Precision and Allan standard deviation

We have performed a basic assessment of the instrument by measuring gas from a high-pressure cylinder containing 1.78 ppm CH_4 for 18 h. We have computed the Allan variance (Allan, 1966) of the resulting data set, using the following definition:

$$\sigma^2(\tau) = \frac{1}{2N}\sum_{i=1}^{N}\left[y(\tau)_{i+1} - y(\tau)_i\right]^2. \quad (1)$$

In this expression, $y(\tau)_i$ are sequential block averages over time τ. The Allan standard deviations (the square root of the Allan variance) for $\delta^{13}CH_4$, CH_4, and C_2H_6 are shown in Fig. 2. The noise isotope ratio and ethane at 1 min of averaging is below 1.0 ‰ and 25 ppb, respectively, and continue to follow a square root averaging law to about 1 h or more.

2.4 Calibration

2.4.1 $^{12}CH_4$

The spectroscopic line used to quantify $^{12}CH_4$ is the same as that used in several widely deployed instruments produced by the same manufacturer (e.g., models G2301 and G2401). The spectroscopy and analysis codes are identical, apart from two small differences:

1. The operating pressure differs by 8 Torr i.e., 148 Torr in this instrument vs. 140 Torr in the other models.

2. The absorption line used to quantify water vapor is different between this model and the other instrumentation

These two differences lead to small differences in the $^{12}CH_4$ calibration factors and the coefficients used to report and correct for water vapor in the gas stream. These effects are investigated below.

The output of the spectroscopic fitting algorithm is a peak height of a line (or lines) associated with the analyte gas. The function relating the mole fraction c to the absorption peak area is linear, according to the Beer–Lambert law. The peak height α does not always vary linearly with gas concentration, but in most situations in near-infrared resolved rovibrational optical spectroscopy, the relationship is substantially linear:

$$c_{12} = k_{12}\alpha_{12} + \varepsilon_{12}. \quad (2)$$

The constant of proportionality k_{12} relates the measured absorption peak height α_{12} to the mole fraction of $^{12}CH_4$ in the sample gas c_{12}, with an offset term ε_{12}. In the absence of other background gas effects (a topic discussed fully below), k_{12} is a constant κ_{12} that is equal to 4.333 ppb $^{12}CH_4$ per ppb cm^{-1} of loss[1], determined by performing a measurement of a calibrated tank with a single instrument (model G2132-I, serial number FCDS2016, Picarro, Inc., Santa Clara, USA). The analytical accuracy of the gas mixture in this tank is 1 %. While this degree of accuracy (20 ppb at 2000 ppb of CH_4) is insufficient for global methane measurements, it is adequate

[1] ppb cm^{-1}, or parts per billion per centimeter, is a unit that describes optical absorbance as a fractional loss of optical power per unit distance.

for the purposes of this study in which the typical methane enhancement was higher than 1000 ppb. For more demanding applications, the instrument can be calibrated using standard gas mixtures with lower uncertainty, which also allows one to determine the offset term ε_{12} which is typically within a few parts per billion of zero.

2.4.2 $\delta^{13}CH_4$

The $^{13}CH_4$ concentration is determined from the measured absorption peak height, using a similar treatment as for $^{12}CH_4$. We begin with the simple linear relationship:

$$c_{13} = k_{13}\alpha_{13} + \varepsilon_{13}. \quad (3)$$

In principle, with careful measurements, we could determine calibration constants for $^{13}CH_4$ as was done for $^{12}CH_4$. However, we have chosen a strategy of selecting $\delta^{13}CH_4$ as the primary isotopic measurement output, rather than $^{13}CH_4$, for the following reasons:

1. It is experimentally more straightforward to generate a constant $\delta^{13}CH_4$ in a varying background gas mixture than it is to generate a constant $^{13}CH_4$ mixture.

2. Dilution by other gas species, such as water vapor, oxygen, or argon, occurs to both species equally (as a percentage of each species' dry mole fraction), which means that $\delta^{13}CH_4$ is unaffected by dilution.

3. Spectral line shape effects due to other gas species are likely to have similar effects on the two methane species. $\delta^{13}CH_4$ is affected only by differences in the line shape effects between the two species.

4. $\delta^{13}C$ is commonly reported on the Vienna Pee Dee Belemnite scale (Coplen et al., 2006), for which there are traceable primary standards. In contrast, there are no independent primary standards for $^{13}CH_4$; the scale for $^{13}CH_4$ is typically defined by a combination of the $\delta^{13}CH_4$ standard and the total CH_4 scale.

Throughout this paper, we will consider $^{12}CH_4$ and $\delta^{13}CH_4$ as the independently calibrated quantities. The individual concentration $^{13}CH_4$ will be derived directly from these two analytical values using the following expression:

$$\delta^{13}CH_4[\text{in ‰}] \equiv 1000\left(\frac{r_{\text{sample}}}{r_{\text{VPDB}}} - 1\right), \quad (4)$$

where $r_{\text{sample}} = c_{13}/c_{12}$ and $r_{\text{VPDB}} = 0.0111802$. The value for r_{VPDB} follows Werner and Brand (2001). Substituting the simple linear relationships for c_{12} and c_{13} (Eqs. 2 and 3) into this expression, we find

$$\delta^{13}CH_4 = 1000\left(\frac{k_{13}\alpha_{13} + \varepsilon_{13}}{(k_{12}\alpha_{12} + \varepsilon_{12})\, r_{\text{VPDB}}} - 1\right). \quad (5)$$

Equation (5) relates the spectroscopic measurements of absorption loss at the peak of the two isotopologues (α_{12} and α_{13}), the calibration coefficients (k_{12} and k_{13}), and the calibration offsets (ε_{12} and ε_{13}) to the determination of $\delta^{13}CH_4$.

First, we consider the case of an ideal spectrometer, for which the calibration coefficients are constants (i.e., $k_{12} = \kappa_{12}$ and $k_{13} = \kappa_{13}$), and the calibration offsets are zero (i.e., $\varepsilon_{12} = \varepsilon_{13} = 0$). These assumptions lead to the following expression, as expected:

$$\delta^{13}CH_4 = 1000\left[\frac{\left(\frac{\kappa_{13}\alpha_{13}}{\kappa_{12}\alpha_{12}}\right)}{r_{\text{VPDB}}} - 1\right]. \quad (6)$$

Equation (6) can be used to calibrate the instrument, as it relates the spectroscopically measurable quantities (i.e., the peak height ratio $\frac{\alpha_{13}}{\alpha_{12}}$) to $\delta^{13}CH_4$. The factory calibration for this set of spectroscopic lines was obtained using the following method. A single bottle of 100 ppm methane (Air Liquide America Specialty Gases, Plumsteadville, Pennsylvania, USA) was used as a source gas. Several 1 L sampling bags (Cali-5-Bond™, Calibrated Instruments, Hawthorne, NY, USA) were filled with the source gas. The bags were equipped with a silicone septum mounted directly on the bag. Pure $^{12}CH_4$ (99.9 atom %, no. 490210, Sigma Aldrich, St. Louis, MO, USA) was injected through the septum in varying amounts to each bag to shift the isotope ratio in the samples. These bags were then measured on an instrument (serial number FCDS002) after diluting 10 : 1 with methane-free zero air, and then these bags were subsequently sent for analysis at a commercial laboratory (Isotech, Champaign, Illinois, USA). Figure 3 shows these calibration data. The samples cover a relatively narrow range of delta, from −60 to −67 ‰. By fitting the data to a line of the form

$$\left[\delta^{13}CH_4\right]_{\text{standard}} = A\frac{\alpha_{13}}{\alpha_{12}} + B, \quad (7)$$

we obtain $A = 165{,}595.70$ ‰ and $B = -1053.59$ ‰. These calibration constants have been transferred to all subsequent instruments.

To validate the calibration over a wider range of delta, we used four isotope standards at a concentration of 2500 ppm CH_4 in a balance of air (Isometric Instruments, Victoria, British Columbia, Canada), with isotope ratios ranging from −66.5 to −23.9 ‰, and an uncertainty of ±0.2 ‰ (as quoted by the supplier). These standards were diluted with zero air using the setup shown in Fig. 4. For each isotope standard, four concentration steps were generated by changing the flow in the mass flow controller (MFC), with the output concentration ranging from 2 to 20 ppm. The values reported by the instrument were generated using the standard instrument calibration constants (i.e., $A = 165,595.70$ ‰ and $B = -1053.59$ ‰). The top panel of Fig. 5 shows the resulting data, along with a linear fit (green line) and the standard calibration (red dashed line). The new instrument calibration

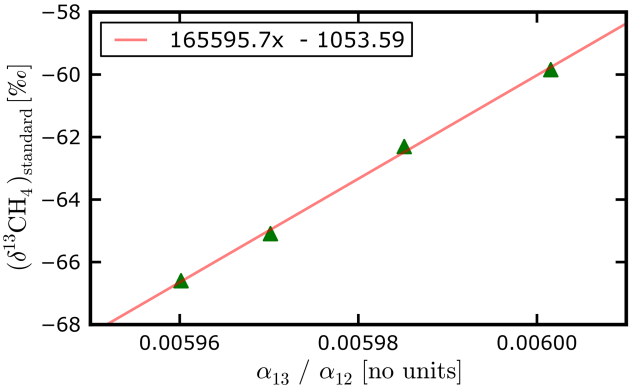

Figure 3. Isotope calibration experiment, using samples prepared for this work and then analyzed at a commercial isotope laboratory. The x axis shows the raw loss ratio provided by the instrument, and the y axis are the results of the external analysis. The linear fit coefficients have been applied to all CRDS instruments that use these spectroscopic lines for $\delta^{13}CH_4$ quantification.

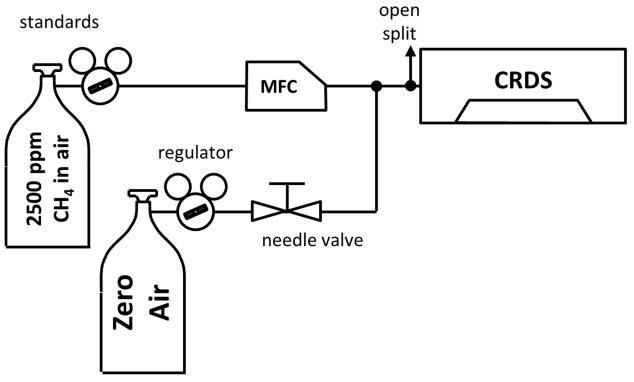

Figure 4. Setup for measuring dilute mixtures of 2500 ppm standards. The MFC was set to flows ranging from 2 to 20 sccm. The needle valve was set to ∼ 1000 sccm dilution, for a concentration range of 2–20 ppm delivered to the instrument.

is given by the constants

$$A' = 153,947‰ \text{ and } B' = -983.29‰. \quad (8)$$

This calibration has a 7 % difference in slope from the initial calibration. The bottom panel shows the residuals of the linear fit (green circles), as well as the difference between the original calibration and the standard values (red values). The two calibration functions give results that are in reasonably good agreement in the −55 to −35 ‰ range. Given the much wider range of these calibration standards, this later calibration is likely to be more accurate in the high and low delta ranges. Results in this paper are reported against the scale defined by these four isotopic ratio standards.

Note that it is recommended that each instrument of this model be calibrated separately and independently, over the relevant range of delta that will be encountered in the experiment, and with sufficient frequency in time (daily or even more frequently) to track any drift in the analyzer. This topic will be discussed in greater detail below.

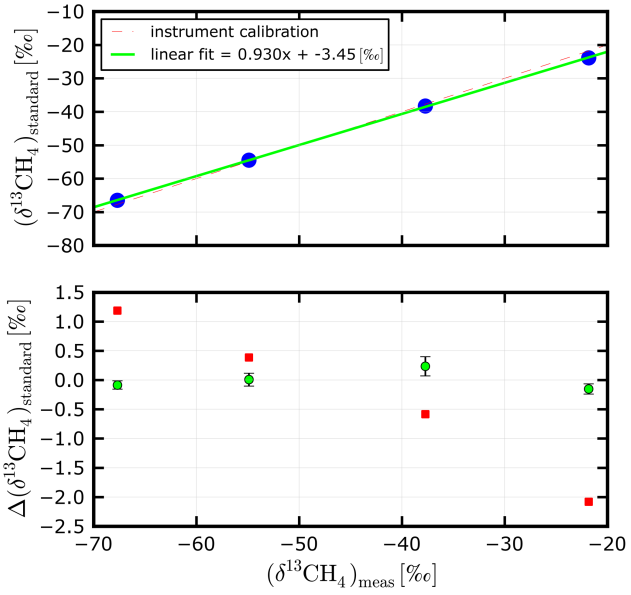

Figure 5. Results of the validation calibration experiment. Top panel: blue circles: measured isotope ratio (x values) vs. standard values from the vendor. Green line: linear fit to these data. Red dashed line: standard instrument calibration ($A = 165,595.7$ and $B = -1053.61$), and including the loss nonlinearity term β and an optimized overall loss offset α_0 of -0.0103 ppb cm^{-1}. Bottom panel: green circles: residuals from the green line in the top panel. The error bars indicate the standard deviation of the four concentration measurements between 1.9 and 15 ppm for each isotope standard, but do not include the uncertainty in the standard value of 0.2 ‰. Red squares: difference between the measured value using the standard instrument calibration and the standard value.

The calibration slope parameter A' can be used to infer the peak height ratio $\frac{\kappa_{13}}{\kappa_{12}}$ from the expression $A' = \frac{1000\left(\frac{\kappa_{13}}{\kappa_{12}}\right)}{r_{VPDB}}$, obtained from inspection of Eqs. (6) and (7). Given $r_{VPDB} = 0.0111802$, we find that $\frac{\kappa_{13}}{\kappa_{12}} = 1.7212$ which means that $\kappa_{13} = 7.458$ ppb of $^{13}CH_4$ per ppb cm^{-1} of loss. For $\delta^{13}CH_4 = 0.0$ ‰, the $^{13}CH_4$ line is 154 times smaller than the $^{12}CH_4$ line.

2.5 Instrument drift and methods for correction

To design an effective calibration and drift correction routine, it is important to understand how the optical spectrometer drifts, and how best to correct for that drift. In Sect. S1 in the Supplement, we present the nonlinearity of the instrument as a function of methane concentration in detail. We begin by inspecting Eq. (S5, in the Supplement), reproduced below

(where we have not included the nonlinear term γ):

$$\left\{\delta^{13}\mathrm{CH_4}\right\}_{\text{spectr., corr}} = \frac{1000}{r_{\mathrm{VPDB}}}\left[\frac{k_{13}\alpha_{13}}{k_{12}\alpha_{12}} + \frac{\alpha_0}{\alpha_{12}}\right] + \left(\frac{1000}{r_{\mathrm{VPDB}}}\frac{k_{13}}{k_{12}}\beta - 1000\right). \quad (9)$$

As has been discussed in the Supplement, the net loss offset term α_0 is due to imperfections in the spectrometer response. There is no reason to assume that these imperfections are constant in time – we therefore include an explicit dependence of this term on time, or $\alpha_0(t)$. There are also spectrometer drifts and errors that can affect the calibration coefficients k_{12} and k_{13}. Examples of this type of drift are cavity temperature or pressure drifts, where the changes are manifest in the absorption cross sections and line shapes. Drift in the laser wavelength reported by the wavelength monitor also tends to cause errors in the measured peak height that is proportional to the peak height, and therefore affect k_{12} and k_{13}. We will assume that the drift in the ratio of the slope coefficients takes on the form $\frac{k_{13}}{k_{12}} = (1+\chi(t))\frac{\kappa_{13}}{\kappa_{12}}$, where $\chi(t)$ is small. Finally, the term β quantifies the degree to which the $^{13}CH_4$ loss measurement α_{13} is dependent of the concentration of $^{12}CH_4$ (α_{13} is independent of $^{12}CH_4$ when $\beta = 0$. To capture potential drift in this term, we will include an explicit dependence of the term β on time: $\beta(t) = \beta_0(1+b(t))$. We do not expect the physical processes that lead to a nonzero β (i.e., nonlinearity in the absorbance axis and crosstalk between $^{12}CH_4$ and $^{13}CH_4$, as described in the Supplement) to drift significantly over time compared to the other two terms, but we include it for completeness. Keeping terms to first order in $\chi(t)$ and $b(t)$, we find

$$\left[\delta^{13}\mathrm{CH_4}\right]_{\text{true}} = 1000\left[\frac{\left(\frac{\kappa_{13}\alpha_{13}}{\kappa_{12}\alpha_{12}}\right) + \chi(t)\left(\frac{\kappa_{13}\alpha_{13}}{\kappa_{12}\alpha_{12}}\right) + \frac{\alpha_0(t)}{\alpha_{12}}}{r_{\mathrm{VPDB}}}\right] + \left(\frac{1000}{r_{\mathrm{VPDB}}}\frac{\kappa_{13}}{\kappa_{12}}\beta_0 - 1000\right) + \frac{1000}{r_{\mathrm{VPDB}}}\frac{\kappa_{13}}{\kappa_{12}}\beta_0(\chi(t)+b(t)). \quad (10)$$

If we substitute in this equation the calibration terms A' and B' and regroup, we arrive at the following expression:

$$\left[\delta^{13}\mathrm{CH_4}\right]_{\text{true}} = A'\frac{\alpha_{13}}{\alpha_{12}} + B' + \frac{c_0(t)}{c_{12}} + \chi(t)A'\frac{\alpha_{13}}{\alpha_{12}} + C'(t), \quad (11)$$

where $A' = \frac{1000\left(\frac{\kappa_{13}}{\kappa_{12}}\right)}{r_{\mathrm{VPDB}}}$, $B' = \left(\frac{1000}{r_{\mathrm{VPDB}}}\frac{\kappa_{13}}{\kappa_{12}}\beta_0 - 1000\right) = A'\beta_0 - 1000$, $c_0 = \frac{1000\kappa_{12}\alpha_0}{r_{\mathrm{VPDB}}}$, and $C'(t) = A'\beta_0(\chi(t)+b(t))$.

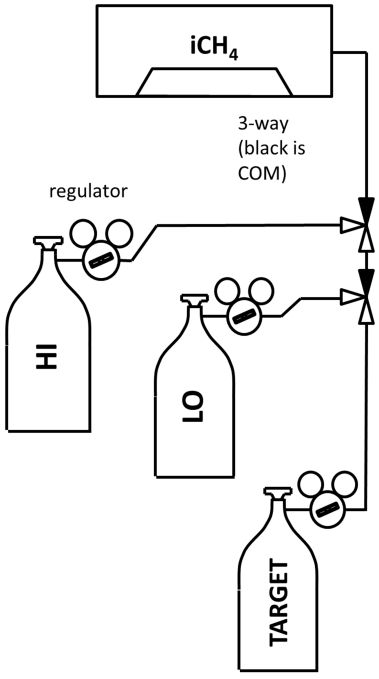

Figure 6. Setup for drift correction testing.

Noting that $A'\frac{\alpha_{13}}{\alpha_{12}} + B' = \left[\delta^{13}\mathrm{CH_4}\right]_{\text{raw}}$, this simplifies to

$$\left[\delta^{13}\mathrm{CH_4}\right]_{\text{true}} = \left[\delta^{13}\mathrm{CH_4}\right]_{\text{raw}} + \frac{c_0(t)}{c_{12}} + \chi(t)\left(\left[\delta^{13}\mathrm{CH_4}\right]_{\text{raw}} - B'\right) + C'(t). \quad (12)$$

Equation (12) shows that as the spectrometer drifts, changes in $c_0(t)$, $\chi(t)$, and $C'(t)$ manifest as three drift terms: one term that is proportional to $\left[\delta^{13}\mathrm{CH_4}\right]_{\text{raw}} - B'$ (a term which is approximately proportional to the ratio of the loss ratio $\frac{\alpha_{13}}{\alpha_{12}}$, as can be seen from Eq. (7), and thus the ratio c_{13}/c_{12}); one term that is inversely proportional to the methane concentration c_{12}, and a simple offset term $C'(t)$that depends on neither concentration nor delta. We recall that variability of the terms $c_0(t)$, $\chi(t)$, and $C'(t)$ is driven by different physical processes (i.e., spectral variations in the optical loss of the empty cavity; errors in the temperature or pressure of the gas, or changes in the wavelength calibration; and changes in the crosstalk between the two methane isotopologues, respectively). We take advantage of these differences to devise a method of drift correction in the next section.

2.5.1 Two-bottle drift correction testing

In this section we describe an experiment in which we track the drift of the instruments using two bottles. In this experiment, we will ignore the contribution of the term $C'(t)$. The two remaining drift terms $c_0(t)$ and $\chi(t)$ have a markedly different dependence on concentration. Therefore, to effec-

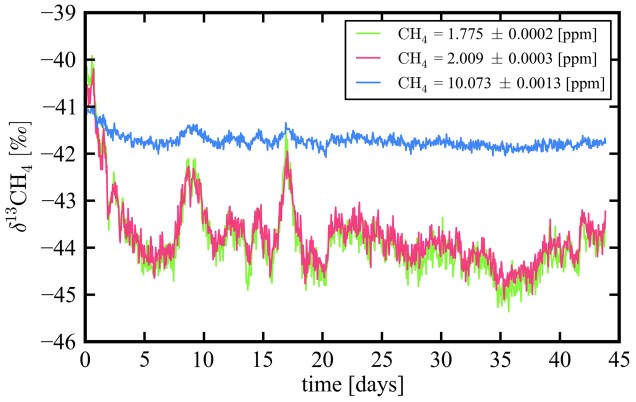

Figure 7. Measured isotope ratio on three bottles, HI (10.1 ppm CH_4 and $\delta^{13}CH_4 = -41.7$ ‰, blue line), LO (1.78 ppm and $\delta^{13}CH_4 = -44.5$ ‰, green line), and Target (2.01 ppm, unknown isotope ratio, red line).

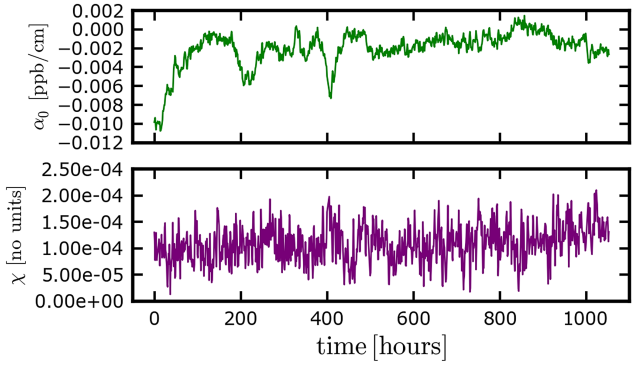

Figure 8. Measurements of the drift correction parameters $\chi(t_i)$ (bottom panel) and $\alpha_0(t_i)$ (top panel), measured from the HI and LO bottles as described in the text. At 2 ppm CH_4, the parameter $\alpha_0(t_i)$ dominates the drift.

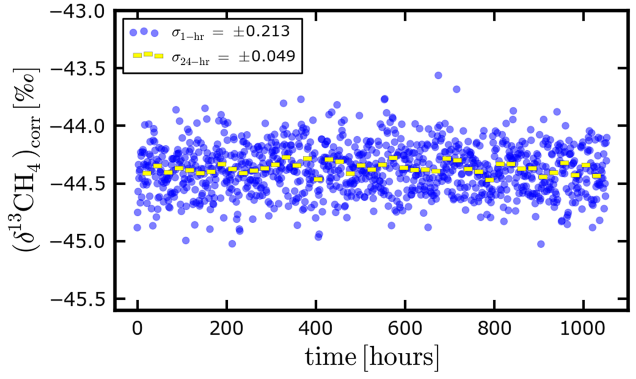

Figure 9. Hourly measurements of $\delta^{13}CH_4$, after correction. The standard deviation of the hourly measurements (blue circles) and the daily measurements (yellow bars) are shown in the figure legend.

tively track drift, we will use two bottles with different CH_4 concentrations. Note that a more accurate calibration scheme would be to track the term $C'(t)$ by employing a third bottle with a substantially different isotope ratio than at least one of the first two bottles. Although the algebra becomes more complicated, the outcome is similar to calibration using two bottles.

There are two bottles in the experiment we performed, shown in Fig. 6: a high concentration bottle (HI) of about 10 ppm CH_4 and $\delta^{13}CH_4 = -41.7$ ‰ and a low concentration bottle (LO) of about 1.8 ppm and $\delta^{13}CH_4 = -44.5$ ‰. A third unknown bottle at about 2 ppm was used as a target tank to quantify the performance of the system. During each hour, 10 min were spent measuring the HI tank, 25 min for the LO tank, and 25 min for the Target tank. This cycle was repeated every hour for 40 days using a single instrument and a single set of tanks.

Figure 7 shows the isotope ratios measured by the instrument for each of the three bottles over time. Clearly, there is significant drift in the instrument. The lower concentration bottles drift much more than the high concentration (about 5 vs. 1 ‰), indicating that $c_0(t)$ is the dominant source of drift in these data.

For each cylinder (HI and LO) measurement during each hour, we may derive an equation based on Eq. (12) that describes the terms $\chi(t_i)$ and $c_0(t_i)$:

$$\delta_{HI} = \delta_H(t_i) + \chi(t_i)\,(\delta_H(t_i) - B) + \frac{c_0(t_i)}{c_{12_H}}, \qquad (13)$$

$$\delta_{LO} = \delta_L(t_i) + \chi(t_i)(\delta_L(t_i) - B) + \frac{c_0(t_i)}{c_{12_L}}.$$

In the above expressions, $\delta_L(t_i) \equiv \left[\delta^{13}CH_4\right]_{\text{raw-LO}}(t_i)$ and $\delta_H(t_i) \equiv \left[\delta^{13}CH_4\right]_{\text{raw-HI}}(t_i)$, and $\delta_{HI,LO}$ are the isotope assignments for each tank.

In addition, we define

$$\Delta_H \equiv \delta_{HI} - \delta_H(t_i) \text{ and } \Delta_L \equiv \delta_{LO} - \delta_L(t_i) \qquad (14)$$

Using these definitions and Eq. (13), we can derive the time-dependent drift parameters $\chi(t_i)$ and $c_0(t_i)$:

$$c_0(t_i) = \frac{\left[\Delta_H(\delta_L(t_i) - B) - \Delta_L(\delta_H(t_i) - B)\right]}{\left[\frac{(\delta_L(t_i)-B)}{c_{12_H}} - \frac{(\delta_H(t_i)-B)}{c_{12_L}}\right]}, \qquad (15)$$

$$\chi(t_i) = \frac{\left[\Delta_H - \frac{c_0(t_i)}{c_{12_H}}\right]}{(\delta_H(t_i) - B)}.$$

In other words, for each hour, we can determine the calibration factors $\chi(t_i)$ and $\alpha_0(t_i)$ from isotope and $^{12}CH_4$ loss measurements of each tank. Figure 8 displays these calibration factors determined from each hourly cycle over the 40 day duration of the experiment. The primary source of drift is the term $c_0(t_i)$, although $\chi(t_i)$ also drifts to a small extent.

Using these calibration constants, we can calculate $\left[\delta^{13}CH_4\right]_{\text{true}}$ on an hourly basis, using Eq. (12), which is

Table 1. Summary of cross-interference due to direct absorption on $\delta^{13}CH_4$ from a variety of species. Reported as a slope for linear cross-interference, and as a range (95 % coverage factor) for nonlinear cross-interference over a specified range of concentration of the interfering species. A positive sign indicates that the value of $\delta^{13}CH_4$ reported by the instrument is more positive than the actual value. See the text for more information.

Gas species	Chemical formula	Estimated effect on $\delta^{13}CH_4$	Notes
Oxygen	O_2	$+0.173 \pm 0.023$ ‰ $\%^{-1}$ O_2	Independent of CH_4 concentration
Argon	Ar	$\approx +0.4$ ‰ $\%^{-1}$ Ar	Independent of CH_4 concentration; estimated from O_2 dependence, using Nara et al. (2012)
Water vapor	H_2O	$< \pm 1$ ‰	0–2.5 % H_2O and 1–15 ppm CH_4
Carbon dioxide	CO_2	$< \pm 0.5$ ‰	200–1800 ppm CO_2 and 1–15 ppm CH_4
Ethane	C_2H_6	$+35$ ‰ ppm CH_4 (ppm C_2H_6)$^{-1}$	Inversely proportional to CH_4 concentration
Ammonia*	NH_3	-7.0 ‰ ppm CH_4 (ppm NH_3)$^{-1}$	Inversely proportional to CH_4 concentration
Hydrogen sulfide	H_2S	< 0.2 ‰ ppm CH_4 (ppm H_2S)$^{-1}$	Inversely proportional to CH_4 concentration
Methyl mercaptan	CH_3SH	< 6 ‰ ppm CH_4 (ppm CH_3SH)$^{-1}$	Inversely proportional to CH_4 concentration
Propane	C_3H_8	< 0.1 ‰ ppm CH_4 (ppm C_3H_8)$^{-1}$	Inversely proportional to CH_4 concentration
Butane	C_4H_{10}	< 0.1 ‰ ppm CH_4 (ppm C_4H_{10})$^{-1}$	Inversely proportional to CH_4 concentration
Ethylene	C_2H_4	$+20$ ‰ ppm CH_4 (ppm C_2H_4)$^{-1}$	Inversely proportional to CH_4 concentration
Carbon monoxide	CO	< 0.02 ‰ ppm CH_4 (ppm CO)$^{-1}$	Estimated from HITRAN database (Rothman et al., 2013)

* Ammonia also has a known strong cross-interference on the ethane measurement.

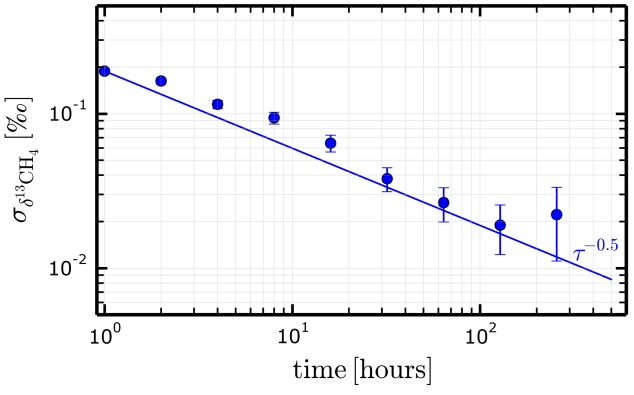

Figure 10. Allan standard deviation of $\delta^{13}CH_4$ after correction, using the data in Fig. 16. The $\tau^{-1/2}$ line is shown for reference, indicating that the noise is nearly random, at least over 100 h. There is a perceptible increase in the Allan standard deviation at about 12 h, which may indicate a moderate dependence of $\delta^{13}CH_4$ on the diurnal cycle. The error bars are estimated based upon the averaging time and the time duration of the data set.

shown in Fig. 9, along with the 24 h average of these data, with standard deviations of ± 0.21 and ± 0.05 ‰, respectively. This stability is comparable to the measurement stability of $\delta^{13}CH_4$ achieved by a high-quality isotope laboratory (Lowe et al., 2002). We have calculated the Allan standard deviation of these data (Fig. 10) in the same way as described in Sect. 2.3. Unlike the raw data, which show increased noise after approximately 1–3 h (Fig. 2), the Allan standard deviation of the calibrated data follows a $\tau^{-1/2}$ law past 100 h of averaging, indicating that the instrument calibrated in this manner is stable over long periods of time. Given this degree of stability, and if care is taken to ensure a somewhat stable environment, we expect that with a properly crafted calibration scheme this instrument can be used for long-term (months or years) in situ atmospheric monitoring of $\delta^{13}CH_4$.

2.6 Cross-interference from other species

It is clearly important that for the instrument to be of practical use, it must precisely and accurately report the analytic quantities ($^{12}CH_4$ and $\delta^{13}CH_4$) over a wide range of variability in the background gas matrix, especially including species such as H_2O and CO_2, which are known to vary significantly in practical field situations. As is clear from Fig. 1, the near-infrared spectra of the key analyte species are not free of spectral interference from other rovibrational absorption lines due to these gas species and other atmospheric constituents. In an ideal spectrometer, using ideal model functions that perfectly describe the absorption spectrum of the gas mixture present in the flow cell, the analysis of the spectra will in principle reproduce the mole fractions of the analyte gas without loss of fidelity. In the real world, however, there are practical limitations to the quality of the spectroscopic model underlying the measurements, which leads to unwanted biases in the reported analyte concentrations as the background gas matrix varies. We call these biases cross-interferences. In Sect. S1, we present in detail the cross-interferences on $^{12}CH_4$ and $\delta^{13}CH_4$ by a variety of atmo-

spheric constituents. The results of this work are summarized in the Table 1. We discuss each species from the table below.

2.6.1 Oxygen and argon

These two gas species do not have any direct spectroscopic absorption in the spectral regions used in the analyzer to quantify methane. They affect the reported methane as a shift in the reported isotope ratio that is proportional to the concentration of the gas. This shift is independent of the methane concentration. Note that the balance gas is nitrogen in these experiments. We note that while it is possible for argon or other inert gases (e.g., helium) to be present in natural gas plumes, we expect that the low concentrations that would be present in the dilute downwind plume to affect the isotope ratio measurement negligibly.

2.6.2 Water vapor and carbon dioxide

These two gas species have direct absorption features that are in the vicinity of the $^{12}CH_4$ and $^{13}CH_4$ absorption lines; these features are incorporated in the spectral models that are used to fit the measured absorption spectra. To the extent that the models are perfect, there would be no cross-interference with $\delta^{13}CH_4$. Experimentally, we find that there are some small deviations in $\delta^{13}CH_4$, especially due to water (these experiments are discussed in greater detail in the Supplement). The impacts of water vapor and carbon dioxide on the isotope ratios are nonlinear in the contaminant gas concentration. In the table, we note the range of isotope ratios that captures 95 % of the observed variability under varying contaminant gas conditions, as noted in the far right column of the table. For the most accurate results, we conclude that the gas stream should be dried to < 0.1 % mole fraction of water vapor prior to analysis, and that the variability of carbon dioxide be limited if possible.

2.6.3 Ethane, ammonia, hydrogen sulfide, methyl mercaptan, propane, butane, ethylene

We have investigated the effect of these gases on the measurement of $\delta^{13}CH_4$. The primary effect that these gases have is to distort the measured absorption spectrum, which in turn leads to an error in the measurement of $\delta^{13}CH_4$. The magnitude of this effect is proportional to the mole fraction of the contaminant species, and inversely proportional to the methane concentration (because at higher methane concentrations, a given distortion of the spectrum has a smaller effect on the isotope ratio). For example, 0.3 ppm of ethane in a gas stream of 3 ppm of CH_4 would shift the $\delta^{13}CH_4$ measurement higher by $[+35\,‰\,\text{ppm}\,CH_4\,(\text{ppm}\,C_2H_6)^{-1}] \times [0.3\,\text{ppm}\,C_2H_6]/[3\,\text{ppm}\,CH_4] = +3.5\,‰$.

2.6.4 Carbon monoxide

The effect of carbon monoxide was not measured (as was the case of the above gases), but estimated from the spectral database HITRAN (Rothman et al., 2013). The spectroscopy of this simple molecule is extremely well understood. Our spectroscopic modeling shows that at the same concentration as methane, the effect on the measured isotope ratio is expected to be negligible. The effect could be more pronounced in an atmosphere rich in carbon monoxide.

3 Experimental methods

3.1 The mobile methane and ethane laboratory

For the experiments in the Uintah Basin, a small consumer sport utility vehicle is used as the mobile platform. An instrument (G2132-i, SN FCDS2004) is placed in the rear compartment of the vehicle. Power is supplied directly from the vehicle's 12V DC electrical system via heavy gauge cables attached directly to the terminals of the vehicle battery. A 1000 W capacity DC to AC modified sine-wave inverter (Power Inverter 1000W, West Marine, Watsonville, CA, USA) is used to supply power to the instrument, pumps, and other equipment in the vehicle. For safety, 40 A DC fuses are placed in line at the battery under the hood of the vehicle, and at the inverter, and care is taken to ensure that all the equipment is properly grounded to the vehicle frame.

A high-precision GPS (R100, Hemisphere GPS, Scottsdale, Arizona, USA) is used for geolocation. The receiver antenna is affixed to the vehicle roof, and the 1 Hz positional data is integrated into the CRDS instrument data stream. A 2-D sonic anemometer is mounted 1.0 m above the roof to be out of the slipstream of the vehicle. Measurements of the wind, transverse and longitudinal to the car's orientation, are also integrated into the instrument data stream. Positional information from the GPS is used to remove the vehicle motion from the measured wind to determine the ground wind velocity.

3.2 Individual source signatures

The mobile laboratory was used to measure the source signatures (i.e., of $\delta^{13}CH_4$ and C_2H_6/CH_4 ratio) of individual emissions sources by directly measuring the composition of the plumes carried downwind of the source location. At driving speeds (5–30 m s^{-1}), typical plumes are traversed in just a couple of seconds. The isotope and ethane measurements are not of sufficient precision to allow for direct analysis of these very fast transients; for this reason, a custom flow system has been designed to allow for fast acquisition and slower reanalysis of atmospheric plumes. This system is shown in Fig. 11. A $\sim$ 4 m long tube is mounted at about 0.15 m above the vehicle roof as the gas inlet, with a flow of about 1900 sccm. The instrument draws about 400 sccm

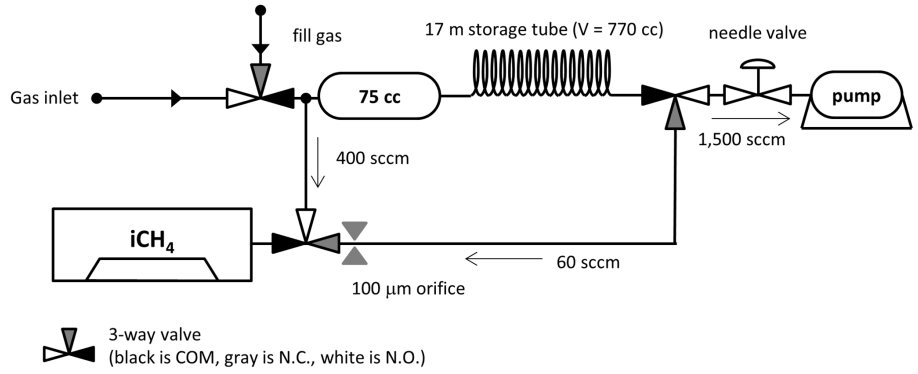

Figure 11. Apparatus for measuring the isotope ratio and ethane-to-methane ratio of single plumes in the mobile lab. For survey mode, all three-way valves are in "normally open" (N.O.) position (white), and the instrument measures the real-time signal at the input to the 770 cc storage tube. The flow through the tube is set by the pump and needle valve. When a plume is detected at the instrument, the three-way valves are switched to "normally closed" (N.C.) position (gray) and the instrument slowly re-analyzes the gas stored in the long tube.

of this gas, and a separate pump (model S2000, Picarro Inc., Santa Clara, CA, USA) is used to draw the remaining gas flow (about 1500 sccm) from this common inlet through a 75 cc mixing volume and then a 15 m long, 8.0 mm I.D. aluminum tube with a volume of 770 cc. The propagation delay in this tube is about 30 s. This long tube is used as a gas storage container that at any point in time contains a gas sample corresponding to the last 30 s of measurements. The software controlling the flow system has two modes of operation. In "survey" mode, the instrument records data directly from the inlet, and the gas flows through the long tube toward the pump at a high flow rate. The software uses an automatic algorithm to detect if the vehicle has just passed through a plume: it identifies whether the concentration has crossed a given peak threshold (typically 1 ppm above background) and returning to within range of the background level (e.g., less than 0.3 ppm above the background level) within 15 s. If these criteria are met, then the flow is automatically switched to "replay" mode. In this case, the flow path is redirected such that the instrument draws directly from the far end of the long tube. The instrument flow is also reduced to about 60 sccm, which is 25 times lower than the survey mode flow through the storage tube. The key aspect of the long tube is that the plume concentration profile is substantially preserved in the tube, because the gas does not diffuse far along the length of the tube during the time of the measurement. This technique is based on a technology called AirCore that was first developed by NOAA as a simple and effective way to measure the vertical profile of trace gases in the atmosphere (Karion et al., 2010; Tans, 2009). Once the gas in the tube is consumed (about 10 min), the flow automatically returns to survey mode. The vehicle was generally in motion during this 10 min analysis.

To quantify the isotopic signature of each individual plume, we have followed the analysis described by Miller and Tans (2003), which is analogous to the Keeling analysis performed in Pataki et al. (2003). Both analysis methods rely on a simple two-member mixing model for source and background gas. The data from each plume measurement are analyzed with the following expression:

$$\delta_{obs} c_{obs} = \delta_s c_{obs} - c_{bg}(\delta_{bg} - \delta_s), \quad (16)$$

where δ_{obs} is the observed $\delta^{13}CH_4$ signal, δ_s is the $\delta^{13}CH_4$ value of the source, δ_{bg} is the $\delta^{13}CH_4$ of the background gas, c_{obs} is the observed methane concentration, and c_{bg} is the background methane concentration. Thus, the isotope signature of the source is obtained from a linear fit of the product $\delta_{obs} c_{obs}$ vs. c_{obs}. The ethane signatures of the individual sources were derived from the data from linear regressions of C_2H_6 vs. CH_4 for each plume. Note that the background gas in this analysis (and contained in the AirCore tubing) is the regional air sample at the locale where the plume was measured encountered immediately before and after the plume was traversed in the vehicle. As such, it contains not just continental background air, but also air contaminated by other sources in the region. The advantage of the Miller–Tans analysis for the isotopic signature (and the slope analysis for the ethane to methane ratio) is that variations in this background from site to site do not affect the derived source signature for the plume.

Over a period of 5 days, 56 separate plume analyses were made in the Uintah Basin. Of the 56 individual source measurements, we have discarded measurements for which the uncertainty of the measurement was greater than ±7 ‰ (1-σ), leaving a total of 28 measurements. For each measurement, we used data from the on-board vehicle anemometer (after subtraction of the motion of the vehicle) to determine the wind direction and identify the source of the plume; by comparing to known locations of gas and oil wells (Uintah Map, 2013) we can categorize the sources as oil wells ($N = 7$) or gas wells ($N = 21$). These results are summarized in Fig. 12. From this figure we make two clear observations. First, the observed isotope ratios in the airborne

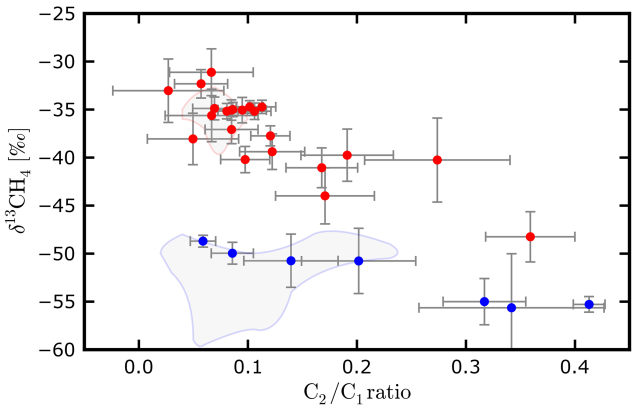

Figure 12. $\delta^{13}CH_4$ and ethane-to-methane ratios for plumes from 21 natural gas wells (red) and seven oil wells (blue) in the Uintah Basin. All of the natural gas measurements were of plumes in the Natural Buttes field in the basin; the oil well measurements were mostly in the Monument Butte field. The natural gas signatures are consistent with previous observations of production gases in the Uintah Basin (Rice et al., 1992), and follow trends observed in other formations for gas associated with oil production and non-associated thermogenic natural gas of various levels of maturation. The red- and blue-outlined gray areas represent distinct populations of wells in the Uintah as described in Rice et al. (1992), for which it has been assumed (for simplicity) that the contribution of propane and heavier alkanes is zero. The centroids of the distribution of gas well signatures are -37.18 ± 3.9 ‰ and 0.118 ± 0.075 for $\delta^{13}CH_4$ and ethane-to-methane ratios, respectively, and for oil, -52.31 ± 2.7 ‰ and 0.223 ± 0.13.

plumes are consistent with the composition of the associated and non-associated gases as described in previous studies in the Uintah Basin (Rice et al., 1992) and from the work of Schoell (1980) and others. This is an important conclusion, as it means that there is not a significant degree of fractionation, either in ethane to methane ratio or in $\delta^{13}CH_4$, associated with the fugitive emission processes that lead to the airborne natural gas plumes. Second, we note that the signature in the vicinity of the gas wells is distinct from the oil well plume signatures. The two populations can be separated using $\delta^{13}CH_4$ (with plumes of > -48 ‰ associated with gas wells), with the difference between the mean of the populations of 15 ‰ equal to 3 times the quadrature sum of the individual standard deviations. We will use the two source signatures in the analysis of the regional atmospheric signal; this analysis is discussed below.

3.3 Regional atmospheric signature

The emissions sources of methane and ethane in the Uintah Basin together with the background concentrations of these gases determine the observed atmospheric signals. We first derive expressions relating the observed atmospheric concentrations and ratios given the background signals and the emissions quantities.

Consider first the emission of methane into the atmosphere. The observed concentration of methane is given by the expression below:

$$c_{\mathrm{obs}} = c_{\mathrm{bg}} + DE_c, \tag{17}$$

where c_{obs} is the observed mole fraction of methane (in absolute units, where e.g., 2 ppm $= 2 \times 10^{-6}$), c_{bg} is the background mole fraction (same units), E_c is the emission rate of methane into the atmosphere, and D is an effective dilution factor for the atmosphere (in units of mole fraction per emission rate). Note that this expression is not exact: the expression holds only when c_{obs}, c_{bg}, and $DE_c \ll 1$. This condition is met under all conditions typically observed in the atmosphere ($c_{\mathrm{obs}} < 2 \times 10^{-5} = 20$ ppm). It is important to note that the term D is not a constant, but can vary over position (due to different spatial distribution of sources upwind of the vehicle) and time (as the atmospheric conditions change).

At any given point in space and time, the term DE_c represents the contribution of all upwind sources to the concentration measured at the point of the observer. The background concentration can be defined in multiple ways, depending on desired observing area or footprint of the measurement. In this paper, we are looking for regional emissions, so we consider the background to be the concentration of methane in the air entering the basin from the upwind direction.

We can write a similar expression to Eq. (17) for the tracer gas (in this case, either ethane or $^{13}CH_4$):

$$e_{\mathrm{obs}} = e_{\mathrm{bg}} + DE_e, \tag{18}$$

where e_{obs} and e_{bg} are mole fractions of the tracer gas for the observations and for background measurements. Note that we have assumed for a given point in space and time that the atmospheric dilution effect and transport (contained in the term D) is the same for the primary gas (methane) and the tracer (ethane or $^{13}CH_4$).

Solving to remove atmospheric dilution from these expressions, we find

$$\frac{e_{\mathrm{obs}} - e_{\mathrm{bg}}}{c_{\mathrm{obs}} - c_{\mathrm{bg}}} = \frac{E_e}{E_c} \equiv r_{\mathrm{s}}, \tag{19}$$

where r_{s} is the overall emission ratio of all sources within the footprint of the observation. In general, we may express this overall source ratio in terms of the emissions of each type of source. In Karion et al. (2013), a study performed in the Uintah Basin, the contribution of cattle and natural seepage to the total methane emissions was estimated to be 2.5 % of production. For the purposes of this analysis, we ignore the contributions of these two sources, leaving two source types: oil wells and gas wells. We decompose the middle term of Eq. (19) into the two source types:

$$\frac{E_e}{E_c} = \frac{E_{e-\mathrm{oil}} + E_{e-\mathrm{gas}}}{E_{\mathrm{oil}} + E_{\mathrm{gas}}} = \frac{\frac{E_{e-\mathrm{oil}}}{E_{\mathrm{oil}}} E_{\mathrm{oil}} + \frac{E_{e-\mathrm{gas}}}{E_{\mathrm{gas}}} E_{\mathrm{gas}}}{E_{\mathrm{oil}} + E_{\mathrm{gas}}}. \tag{20}$$

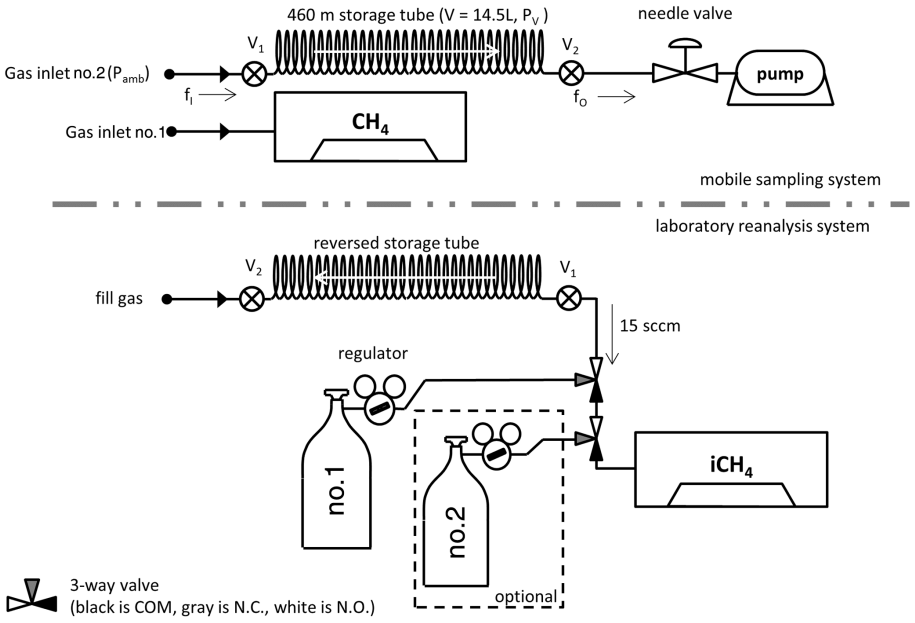

Figure 13. Apparatus for making regional isotope and ethane ratio measurements. The top schematic shows the mobile sampling system. The flow through the long storage tube is set by the pump and needle valve. The two manual valves (V_1 and V_2) are in the open position during the measurements, and closed when the survey is complete. An optional flow meter can be inserted in the line upstream of the storage tube to verify the actual flow into the instrument. An instrument in the vehicle measures the local ambient concentration on a separate inlet. The storage tube is transported to the laboratory (lower schematic), where the gas stored in the long tube is reanalyzed slowly (with the flow reversed, so the last gas in is the first out). The reanalysis is periodically interrupted to run one or more calibration standard. A gas drying system can be introduced downstream of the storage tube in the laboratory to reduce the possible effect of water vapor on the measurements, but this was not done in the results reported here. A fill gas other than ambient air can be used to denote the end of the sample.

In this expression, E_{oil} and E_{gas} are the emission rates of methane from each source type, oil wells and gas wells; similarly, $E_{e-\text{oil}}$ and $E_{e-\text{gas}}$ are the tracer emissions from each source type. Defining $r_{\text{oil}} = \frac{E_{e-\text{oil}}}{E_{\text{oil}}}$ and $r_{\text{gas}} = \frac{E_{e-\text{gas}}}{E_{\text{gas}}}$, we find

$$r_{\text{s}} = \frac{r_{\text{oil}} E_{\text{oil}} + r_{\text{gas}} E_{\text{gas}}}{E_{\text{oil}} + E_{\text{gas}}}. \tag{21}$$

Using Eq. (21), if we can measure r_{s} (the overall ratio of the tracer to methane observed in the atmosphere), and given the source signatures of oil and gas sources r_{oil} and r_{gas} observed in Fig. 12, we can determine the relative fraction of the emissions of oil and gas, without measuring the emission rates directly.

How can we determine the source emission ratio r_{s}? By regrouping terms in Eq. (19), and by defining $r_{\text{obs}} = e_{\text{obs}}/c_{\text{obs}}$ and $r_{\text{bg}} = e_{\text{bg}}/c_{\text{bg}}$, we arrive at the following expression:

$$e_{\text{obs}} = r_{\text{s}} c_{\text{obs}} + \left(r_{\text{bg}} - r_{\text{s}}\right) c_{\text{bg}}. \tag{22}$$

Note that the source emission ratio r_{s} is obtained from the slope of a plot of e_{obs} vs. c_{obs}. This equation is constructed similarly to the Miller–Tans method for isotope analysis (Miller and Tans, 2003). In fact, this equation reduces to the Miller–Tans equation via algebraic manipulation to convert the ratios r_{s}, r_{obs}, and r_{bg} to delta notation via $\delta = 1000\left(\frac{r}{r_{\text{VPDB}}} - 1\right)$:

$$\delta_{\text{obs}} c_{\text{obs}} = \delta_{\text{s}} c_{\text{obs}} + \left(\delta_{\text{bg}} - \delta_{\text{s}}\right) c_{\text{bg}}. \tag{23}$$

These expressions can be used to quantify the source signatures (r_{s} for ethane and $\{\delta^{13}CH_4\}_{\text{s}}$) given the observations and the background values.

To quantify the emission rates of oil wells relative to gas wells, we need a method for collecting a representative sample of the air in the Uintah Basin. We have designed a system that samples gas over long periods of time from the mobile lab. This gas sample is analyzed in a stationary laboratory, where careful calibration and longer measurement times can be brought to bear to improve the precision and accuracy of the measurements of $\delta^{13}CH_4$ and ethane. The sampling system is based on the AirCore concept, but with a much larger volume. The system is shown in Fig. 13. The top schematic shows the sampling system in the vehicle. Real-time measurements of the CH_4 concentration are also made during the drive, along with GPS coordinates and local wind speed and direction. We estimate that by using this larger AirCore we have improved the precision of the regional air measurement by about a factor of 3 relative to the in-vehicle measurement, without the need to carry a compressed air cylinder in the vehicle.

To ensure that the gas sampled in the storage tube is representative of the regional air, it is important to have a good understanding of the inlet flow of the system. Under constant pressure conditions at the inlet of the system, the flow at the inlet f_{in} is equal to the flow at the exit of the long storage tube f_{out}. However, the inlet pressure is not constant while in motion, due to altitude changes and dynamic pressure changes due to the Bernoulli Effect. These pressure changes will lead to flow changes at the inlet of the system, leading to uneven sampling of the regional air. We have constructed a complete air flow model that we have demonstrated matches observations. This model and associated experimental validation is described in the Supplement.

The bottom panel of Fig. 13 shows the laboratory reanalysis system. The reanalysis can occur at a much slower flow rate (about 17 sccm for experiments described here), leading to improved precision on the isotope and ethane analysis, and the overall accuracy and drift of the system is improved by using one or more calibration standards. For the measurements described here, we used a single cylinder at 1.85 ppm CH_4 and -47.5 ± 0.5 ‰ (a bottle of whole air collected and compressed at Niwot Ridge, Colorado) as the single standard. During each reanalysis period, we assumed that the drift of the instrument is in the concentration-dependent term $c_0(t)$ (Eq. 12).

To associate a particular measurement made in the laboratory during reanalysis to a specific location on the drive, it is necessary to properly resynchronize the time axes, and to account for gas diffusion in the tube. This is accomplished using the following procedure:

1. The time axis during the "recording" phase is never adjusted.

2. The reanalysis time axis (called "replay" time) is first shifted by the time delay between the end of the recording and the beginning of the reanalysis.

3. The flow in the storage tube is reversed during reanalysis; for this reason, the replay time axis is reversed.

4. The time axis is compressed by the ratio of reanalysis flow to recording flow (or $17/88$ sccm $= 0.19$).

5. To compare the methane signal measured during reanalysis to the recorded methane signal, a smoothing function is convolved with the recorded methane time series. This smoothing function is simply the Green's function for 1-D diffusion:

$$f(x) = \exp\left(-\frac{x^2}{4Dt_s}\right). \quad (24)$$

In this expression, x is distance along the length of the tube and t_s is the residence time of the gas at the location x, and we have used a diffusion constant $D = 0.2\,\mathrm{cm^2\,s^{-1}}$ (Marrero and Mason, 1972). There are no free parameters in this smoothing function. It is important to note that other than gas diffusion (which conserves total methane), there are no adjustments made to the methane measurements during the recording phase or reanalysis phase.

6. Finally, to account for flow differences in different parts of the drive, the replay time axis is compressed or expanded using a cubic spline function with 15 knots across the time axis (every 300 s), minimizing the time mismatch between the smoothed recorded methane signal and the reanalyzed signal.

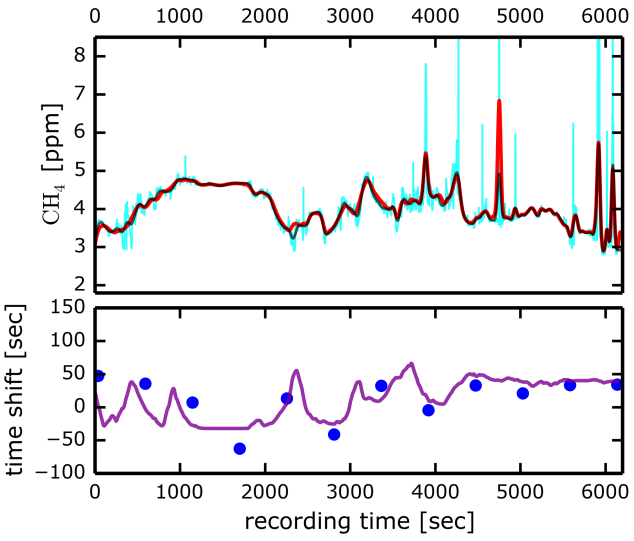

Figure 14. Top panel: cyan denotes the methane signal recorded in the vehicle over about 1.6 h on 3 February 2013. Some individual plumes are as large as 30 ppm. Black denotes the methane signal recorded in the vehicle, after applying the smoothing function derived from gas diffusion in the storage tube. Red denotes the methane signal obtained during reanalysis of the gas stored in the tube over about 24 h of analysis time. The time axis of the reanalyzed signal has been adjusted according to the ratio of the flows during recording and reanalysis. To account for flow differences in different parts of the drive, the replay time axis is compressed or expanded using a cubic spline function with 15 knots across the time axis (every 300 s), optimizing the time mismatch between the recorded methane signal and the reanalyzed signal. These time shifts are shown in the bottom panel (blue points) (where a positive value indicates that the reanalysis time should be shifted later, indicative of a reduced flow into the tube). The purple line in the bottom panel is the time shift predicted by the inlet flow model for this drive described in the Supplement – the only free parameter was an overall offset to the modeled time shift.

The result of this procedure is shown in Fig. 14. The reanalyzed data reproduces the smoothed in-vehicle measurements well, except for the most narrow methane plumes observed during the drive (e.g., at $t = 4800$ s). The mismatch in the vertical axis on these narrow plumes is due to (a) the fact that the instantaneous flow into the sampling tube is highly vari-

able, leading to an under- or overrepresentation of that plume in the sampling tube, and (b) the two inlets are near to each other on the vehicle (within 0.5 m), but do not sample exactly the same location. The agreement between the time shift derived from the methane observations and the time shift predicted from the pressure/flow model (Sect. S2) indicates that the flow model is a good representation of the flow into the system.

Dozens of individual narrow plumes (< 10 s in duration) are visible in Fig. 14. These plumes are due to sources that are relatively close to the vehicle (<∼ 150 m) during the drive. To the extent that these sources are representative of the overall distribution of sources in the region, these individual plumes do not present a problem, but if the sources are atypical, the regional emissions result derived from this analysis could have an error. We estimate the contribution of these individual sources in the regional signal using the following expression:

$$f_{\text{local}} = \frac{\int [C(t) - C_{15}(t)]}{\int [C(t) - C_0]}, \quad (25)$$

where $C(t)$ is the concentration observed during the drive, C_0 is the minimum concentration observed on the drive (2.1 ppm in this case), and $C_{15}(t)$ is the minimum concentration within ±15 s of time t. At our typical driving speeds of 15 m s^{-1}, 15 s corresponds to 225 m of distance; thus, our algorithm defines a "local" source as producing a plume narrower than 225 m. Both integrals are performed over the entire drive. The integral in the numerator is near zero unless the vehicle encounters methane plumes that are narrower than about a minute of drive time. For slowly varying signals, the moving baseline $C_{15}(t)$ reduces the contribution to the integral. The integral in the denominator is used to normalize the signal. If we consider the example of a fairly constant baseline with narrow plumes (e.g., less than 15 s wide), f_{local} will be very close to 100 %. In contrast, a slowly varying methane signal with no narrow plumes will lead to f_{local} near 0 %. Using this expression, we calculate $f_{\text{local}} = 10\,\%$, indicating that 10 % of the observed signal in Fig. 14 is due to local influence, and thus that 90 % of the observed signal is a regional signal. Twenty-one plumes with a peak height greater than 0.5 ppm were identified, with an average amplitude = 5.6 ppm.

A total of three regional drives were performed in the winter of 2013, with a total distance travelled of 314 km. The regional fractions for these drives were 90, 92, and 91 %, for an average of 91 %. For each drive, data from the reanalysis are averaged in 5 min blocks, corresponding to a time resolution of about 1 min, or 1 km along the path of the vehicle. In this way, we obtain values for CH_4, $\delta^{13}CH_4$, and ethane that correspond to these 1 km path segments.

The reanalysis algorithm provides a functional relationship between the time axis of the recorded data to that of the reanalyzed data. Using this relationship, we associate the isotope and ethane signatures measured in the laboratory with the latitude and longitude recorded in the vehicle. A map of the Uintah Basin, showing the locations of gas and oil wells is shown in Fig. 15, along with the recorded isotope signatures for the three drives. A clear geographic dependence of the isotope ratio can be seen, with the heaviest values observed in the primary gas production area in the southeast of the basin, and the lightest values observed in the oil-producing region in the west. The concentration signatures were also highest in the gas-producing area, although, because the data were collected on different days with different atmospheric conditions, direct comparison is difficult.

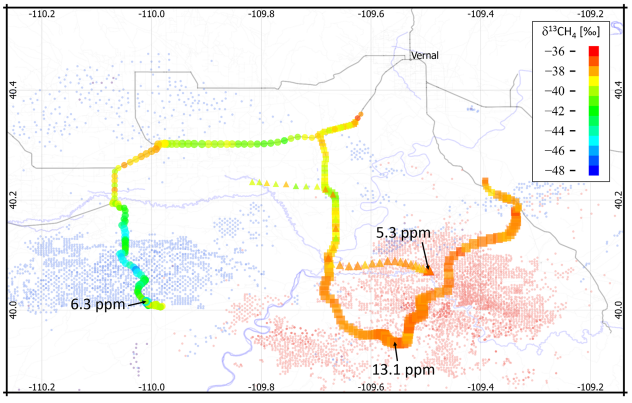

Figure 15. Map of the Uintah Basin, showing the locations of oil wells (blue) and gas wells (red). The axes are in degrees of longitude (x axis) and latitude (y axis). In addition, the gas measurements obtained from the three regional drives are plotted, where the area of the symbol is proportional to the gas concentration above the background level of 1.877 ppm (measured at Niwot Ridge), and the color is given by the isotope ratio, with heavy ratios in red and light ratios in blue. The highest methane concentration for each drive is indicated directly on the figure. Symbols correspond to the date of the measurement (circles: 1 February 2013; squares: 3 February 2013; triangles: 9 February 2013). Concentrations are highest in the primary gas production area in the southeast, and the observed isotope ratio is heavy. Isotope ratios in the oil-producing areas are lightest, and the concentrations are lower. The concentrations have been scaled so that common segments of the drives have the same average concentration (see text for details). Map image generated by Quantum GIS (Quantum, 2013); road and waterways data© OpenStreetMap contributors.

Figure 16 shows a Keeling plot of the observed isotope ratios (left panel) and the ethane-to-methane ratio (right panel) from these drives.

We can make three clear observations from these data:

1. The regional isotope signatures are consistent with the gas wells as the predominant emissions source.

2. The regional ethane-to-methane ratio is about 9.6 %, which is close to the gas source average ratio of 11.8 % (the centroid of the gas well ethane-to-methane ratio from Fig. 12), and significantly different than the oil well signature of 22.3 % (also from Fig. 12), although

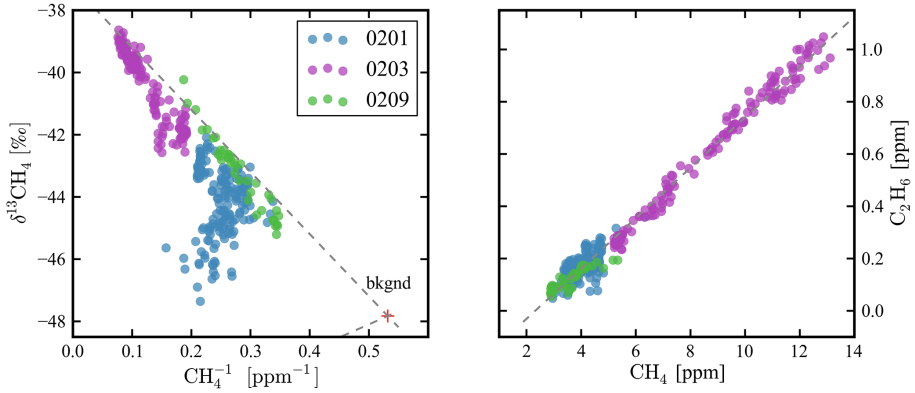

Figure 16. Left panel: Keeling plot of $\delta^{13}CH_4$ vs. $(CH_4)^{-1}$ for the three drives on 1 February (0201), 3 February (0203), and 9 February (0209) in 2013. The point labeled "bkgnd" is the measurement of Niwot Ridge, Colorado, air by NOAA in February 2012: $CH_4 = 1.877$ ppm (Dlugokencky et al., 2015) and $\delta^{13}CH_4 = -47.412$ ‰ (White and Vaughn, 2014). The top gray line indicates a source of gas with a −37.2 ‰ isotope ratio (the centroid of the individual gas sources in Fig. 12), and the bottom gray line indicates a source of −52.3 ‰ (the centroid of the individual oil sources in Fig. 12). Clearly the majority of the observed isotope ratios are dominated by gas sources. Right panel: plot of ethane vs. methane for the same three drives. The gray dashed line follows an ethane-to-methane ratio of 0.096.

we note that the uncertainty in the ethane ratios is very high for both populations (7.5 and 13 %, respectively).

3. Even in the predominantly oil-producing western region (1 February drive), the observed isotope ratio, which shows significant deviation to lighter isotope values, implies that the observed signal is a mixture of nearby oil sources and the more distant gas sources.

Taken together, these observations provide strong evidence that the gas wells are the predominant source of methane in the Uintah Basin. We note that these measurements were purposely made during a period of time when an atmospheric inversion was present in the Uintah Basin. There is only one opportunity for air to flow out of the basin (the Green River valley to the south), and the methane accumulated in the basin atmosphere over several days. It is therefore not surprising that the dominant emissions source signature (in this instance, the gas wells) would be visible throughout the basin, even in the western region.

To quantify the emission ratio, we apply the following algorithm. First, we consider each point in the left panel of Fig. 16, which corresponds to the isotope ratio at a specific location on one of the drives. From this isotope ratio, we can calculate a "local" isotope ratio at any position x on the path of the vehicle from the following expression based on Eq. (21):

$$\delta_s(x) = \frac{\delta_{oil} E_{oil}(x) + \delta_{gas} E_{gas}(x)}{E_{oil}(x) + E_{gas}(x)}. \quad (26)$$

If we define the fraction of emissions from gas wells observed at location x as $R_{gas}(x) = \frac{E_{gas}(x)}{E_{oil}(x)+E_{gas}(x)}$, and using the fact $\frac{E_{oil}(x)}{E_{oil}(x)+E_{gas}(x)} = 1 - \frac{E_{gas}(x)}{E_{oil}(x)+E_{gas}(x)} = 1 - R_{gas}(x)$, we find that $R_{gas}(x) = \frac{\delta_s(x)-\delta_{oil}}{\delta_{gas}-\delta_{oil}}$.

To derive the total regional ratio R_{gas}, we need to perform a weighted sum over all locations in the basin:

$$R_{gas} = \frac{\sum_{allx} R_{gas}(x) E_{tot}(x)}{\sum_{allx} E_{tot}(x)}. \quad (27)$$

It is difficult to quantify the local emissions $E_{tot}(x)$ that contribute to a given regional signature. We do however know the concentration $c(x)$, which is the measured concentration along the path of the vehicle. Can $c(x)$ be used as a proxy for $E_{tot}(x)$? To the extent that the atmospheric dilution term D in Eq. (17) is substantially constant throughout the drive, and that sources are randomly distributed upwind of the vehicle, the measured concentration enhancement $c(x) - c_{bg}$ is a good proxy for the emissions rate, or

$$\mathcal{R}_{gas} = \frac{\sum_{allx} R_{gas}(x)\left(c(x) - c_{bg}\right)}{\sum_{allx}\left(c(x) - c_{bg}\right)}, \quad (28)$$

in which c_{bg} is the background value from which the concentration enhancement occurs. During the atmospheric inversion event, it is difficult to define a specific background value. For the purposes of this analysis, we assign the concentration measured at Niwot Ridge in February 2013 of 1.877 ppm (Dlugokencky et al., 2015) as the background concentration. The small fraction of the concentration enhancement that is due to sources outside the Uintah Basin will then contribute to the overall uncertainty of the emissions attribution; this contribution is difficult to quantify, but is expected to be small given the large enhancements observed in this study. These sources of uncertainty in the background concentration (and isotope ratio) are captured in the Monte Carlo simulation, discussed below.

If we continue to use the assumption that the emissions-weighted end members of gas and oil sources are −37.2 and −57.3 ‰, respectively, we find that the overall emission ratio derived from each of the drives using Eq. (28) is 73, 93, and 91 % for each of the three drives (1, 3, and 9 February 2013). If each of the drives is weighted equally, we find that $\mathcal{R}_{gas} = 0.88$. Alternatively, we take advantage of the fact that we drove certain segments of the drive on multiple days by adjusting the concentrations such that the observed concentration on all the drives are the same in these common segments of the paths. In that situation, $\mathcal{R}_{gas} = 0.85$ where the weighting factors for the three drives are 2.2, 1.0, and 3.6, respectively. Although the difference between the two results is small, we will use adopt this weighting in the uncertainty discussion below.

It is not a surprising result that the majority of methane emissions in the Uintah Basin are from natural gas wells. The 2012 emission study performed in the Uintah (Karion et al., 2013) focused on the gas-producing eastern portion of the basin, but about 1000 of the 3000 oil wells in the basin. The western portion of the flight path used in that study traverses the western oil-producing region. This segment of the flight path does not show a significant methane enhancement, in support of the conclusion that the gas field is the dominant source of methane in the region.

To quantify the uncertainty in the fractional emissions estimate, we perform a Monte Carlo uncertainty analysis, by varying the following parameters (normally distributed) around their nominal values: δ_{gas}, δ_{oil}, δ_{bkgnd}, and c_{bkgnd}. In Karion et al. (2013), no dominant single source of methane was found, in support of the idea that the emissions are due to an ensemble of many sources. We have thus assumed that the individual sources sampled directly are representative of the distribution of sources that comprise the total emissions. The variability in the gas and oil end members is given by the uncertainty in the means of each individual source distributions shown in Fig. 12, or $\frac{\sigma_{std}}{\sqrt{N}}$ (Bevington and Robinson, 1969), assuming that the population of wells sampled is representative of all the wells contributing to the emissions. In addition, we have assumed an uncertainty in δ_{bkgnd} and c_{bkgnd} of 1 ‰ and 0.1 ppm, respectively; the primary source of the uncertainty in the background parameter is due to the fact that because of the atmospheric inversion, it is not possible to define a clear background for the regional enhancements. For this set of parameters, we find that $\mathcal{R}_{gas} = 0.85 \pm 0.07$ (1-σ), where 95 % of the Monte Carlo realizations have $\mathcal{R}_{gas} > 0.75$. The contributions of δ_{gas} and δ_{bkgnd} to the total uncertainty are approximately equal, and together account for 90 % of the total uncertainty of 0.07.

If the isotope ratios of the sources sampled are not representative of the emissions-weighted distribution of well signatures, then uncertainty in the mean of the sampled distribution underestimates the uncertainty in the centroid of the full population. The uncertainty in the end members should be increased to encompass the populations that were not sampled. Assuming that the population is at least somewhat representative, and noting that the observed range in isotope values and ethane ratios is typical of oil- and gas-producing geological formations, then the standard deviation of the sampled distribution should represent a reasonable upper limit for the uncertainty. In this situation, a substantial fraction of the Monte Carlo realizations are nonphysical i.e., the isotope ratios observed in the regional sampling can exceed the simulated gas well end member, leading to calculated emission ratios that exceed 1 at times. However, even with these highly uncertain end member populations, > 98 % of the realizations predict that $\mathcal{R}_{gas} > 0.5$, and 80 % of the realizations indicate that $\mathcal{R}_{gas} > 0.7$.

Finally, we note that the three drives that contributed to this study are not necessarily representative of the total air mass in the basin. We can obtain one estimate of this sampling uncertainty by noting that the drive in the oil-producing region lead to an estimate of 73 % for the emission ratio, and drives in the gas-producing region lead to estimates of 93 and 91 %, for a total span of about ±10 % at most.

4 Summary

In this paper, we present a comprehensive approach to emissions attribution, using an innovative CH_4, $\delta^{13}CH_4$, and C_2H_6 instrument based on cavity ring-down spectroscopy (CRDS). The design and performance of the analyzer is presented in detail. We have demonstrated that with proper calibration, the instrument can deliver high-quality $\delta^{13}CH_4$ measurements with a precision that is comparable to isotope ratio mass spectrometry. The instrument is compact and rugged, and can be deployed in remote field stations or mobile platforms with a minimal amount of user attention.

As an example of the type of research that can be performed with this instrument, field measurements were performed in the Uintah Basin (Utah, USA) in the winter of 2013, using a mobile lab equipped with the CRDS analyzer, a high-accuracy GPS, a sonic anemometer, and an onboard gas storage and playback system. With an extremely small population and almost no other sources of methane and ethane other than oil and gas extraction activities, the Uintah Basin represents an ideal location to investigate and validate new measurement methods of atmospheric methane and ethane. We present the results of measurements of the fugitive emissions from 23 natural gas wells and six oil wells in the region. The $\delta^{13}CH_4$ and C_2H_6 signatures that we observe are consistent with the signatures present in the ground. Furthermore, regional measurements of the atmospheric CH_4, $\delta^{13}CH_4$, and C_2H_6 signatures throughout the basin have been made, using continuous atmospheric sampling into a 450 m long tube. These measurements suggest that 85 ± 7 % of the total emissions in the basin are from natural gas production.

The Supplement related to this article is available online at doi:10.5194/amt-8-4539-2015-supplement.

Acknowledgements. The authors would like to thank Colm Sweeney, Gaby Petron, Anna Karion, Sonja Wolter, Tim Newberger, and Bruce Vaughn for experimental support and helpful scientific discussions during this project.

Edited by: M. Hamilton

References

Allan, D. W.: Statistics of atomic frequency standards, P. IEEE, 54, 221–230, 1966.

Alvarez, R. A., Pacalab, S. W., Winebrake, J. J., Chameides, W. L., and Hamburg, S. P.: Greater focus needed on methane leakage from natural gas infrastructure, P. Natl. Acad. Sci. USA, 109, 6435–6440, doi:10.1073/pnas.1202407109, 2012.

Bevington, P. R. and Robinson, D. K.: Data Reduction and Error Analysis for the Physical Sciences, vol. 336, McGraw-Hill, New York, 1969.

Bräunlich, M., Aballain, O., Marik, T., Jöckel, P., Brenninkmeijer, C. A., Chappellaz, J., and Sturges, W. T.: Changes in the global atmospheric methane budget over the last decades inferred from ^{13}C and D isotopic analysis of Antarctic firn air, J. Geophys. Res.-Atmos., 106, 20465–20481, 2001.

Chen, H., Winderlich, J., Gerbig, C., Hoefer, A., Rella, C. W., Crosson, E. R., Van Pelt, A. D., Steinbach, J., Kolle, O., Beck, V., Daube, B. C., Gottlieb, E. W., Chow, V. Y., Santoni, G. W., and Wofsy, S. C.: High-accuracy continuous airborne measurements of greenhouse gases (CO_2 and CH_4) using the cavity ring-down spectroscopy (CRDS) technique, Atmos. Meas. Tech., 3, 375–386, doi:10.5194/amt-3-375-2010, 2010.

Coplen, T. B., Brand, W. A., Gehre, M., Gröning, M., Meijer, H. A., Toman, B., and Verkouteren, R. M.: After two decades a second anchor for the VPDB $\delta^{13}C$ scale, Rapid Commun. Mass Sp., 20, 3165–3166, 2006.

Crosson, E. R.: A cavity ring-down analyzer for measuring atmospheric levels of methane, carbon dioxide, and water vapor, Appl. Phys. B-Lasers O., 92, 403–408, doi:10.1007/s00340-008-3135-y, 2008.

Dlugokencky, E. J., Nisbet, E. G., Fisher, R., and Lowry, D.: Global atmospheric methane: budget, changes and dangers, Philos. Trans. Roy. Soc. London A, 369, 2058–2072, 2011.

Dlugokencky, E. J., Lang, P. M., Crotwell, A. M., Masarie, K. A., and Crotwell, M. J.: Atmospheric Methane Dry Air Mole Fractions from the NOAA ESRL Carbon Cycle Cooperative Global Air Sampling Network 1983–2014, Version: 2015-08-03, available at: ftp://aftp.cmdl.noaa.gov/data/trace_gases/ch4/flask/surface/, last access: 7 September, 2015.

Edwards, P. M., Young, C. J., Aikin, K., deGouw, J., Dubé, W. P., Geiger, F., Gilman, J., Helmig, D., Holloway, J. S., Kercher, J., Lerner, B., Martin, R., McLaren, R., Parrish, D. D., Peischl, J., Roberts, J. M., Ryerson, T. B., Thornton, J., Warneke, C., Williams, E. J., and Brown, S. S.: Ozone photochemistry in an oil and natural gas extraction region during winter: simulations of a snow-free season in the Uintah Basin, Utah, Atmos. Chem. Phys., 13, 8955–8971, doi:10.5194/acp-13-8955-2013, 2013.

Fang, S.-X., Zhou, L.-X., Masarie, K. A., Xu, L., and Rella, C. W.: Study of atmospheric CH_4 mole fractions at three WMO/GAW stations in China, J. Geophys. Res.-Atmos., 118, 4874–4886, doi:10.1002/jgrd.50284, 2013.

Fisher, R., Lowry, D., Wilkin, O., Sriskantharajah, S., and Nisbet, E. G.: High-precision, automated stable isotope analysis of atmospheric methane and carbon dioxide using continuous-flow isotope-ratio mass spectrometry. Rapid Comm. Mass Spectr., 20, 200–208, 2006.

Fisher, R. E., Sriskantharajah, S., Lowry, D., Lanoisellé, M., Fowler, C. M. R., James, R. H., Hermansen, O., Myhre, C. L., Stohl, A., Greinert, J., Nisbet-Jones, P. B. R., Mienert, J., and Nisbet, E. G.: Arctic methane sources: Isotopic evidence for atmospheric inputs, Geophys. Res. Lett., 38, L21803, doi:10.1029/2011GL049319, 2011.

Kai, F. M., Tyler, S. C., Randerson, J. T., and Blake, D. R.: Reduced methane growth rate explained by decreased Northern Hemisphere microbial sources, Nature, 476, 194-197, 2011.

Karion, A., Sweeney, C., Tans, P., and Newberger, T.: AirCore: an innovative atmospheric sampling system, J. Atmos. Ocean. Tech., 27, 1839–1853, 2010.

Karion, A., Sweeney, C., Pétron, G., Frost, G., Hardesty, R. M., Kofler, J., Miller, B. R., Newberger, T., Wolter, S., Banta, R., Brewer, A., Dlugokencky, E., Lang, P., Montzka, S. A., Schnell, R., Tans, P., Trainer, M., Zamora, R., and Conley, S.: Methane emissions estimate from airborne measurements over a western United States natural gas field, Geophys. Res. Lett., 40, 4393–4397, doi:10.1002/grl.50811, 2013.

Kirschke, S., Bousquet, P., Ciais, P., Saunois, M., Canadell, J. G., Dlugokencky, E. J., Bergamaschi, P., Bergmann, D., Blake, D. R., Bruhwiler, L., Cameron-Smith, P., Castaldi, S., Chevallier, F., Feng, L., Fraser, A., Heimann, M., Hodson, E. L., Houweling, S., Josse, B., Fraser, P. J., Krummel, P. B., Lamarque, J.-F., Langenfelds, R. L., Le Quéré, C., Naik, V., O'Doherty, S., Palmer, P. I., Pison, I., Plummer, D., Poulter, B., Prinn, R. G., Rigby, M., Ringeval, B., Santini, M., Schmidt, M., Shindell, D. T., Simpson, I. J., Spahni, R., Steele, L. P., Strode, S. A., Sudo, K., Szopa, S., van der Werf, G. R., Voulgarakis, A., van Weele, M., Weiss, R. F., Williams, J. E., and Zeng, G.: Three decades of global methane sources and sinks, Nat. Geosci., 6, 813–823, 2013.

Levin, I., Glatzel-Mattheier, H., Marik, T., Cuntz, M., Schmidt, M., and Worthy, D. E.: Verification of German methane emission inventories and their recent changes based on atmospheric observations, J. Geophys. Res., 104, 3447–3456, doi:10.1029/1998JD100064, 1999.

Lowe, D., White, J., Levin, I., Bergamaschi, P., Wahlen, M., and Miller, J.: Isotope measurement techniques for atmospheric methane, in: Stable isotope measurement techniques for atmospheric greenhouse gases, International Atomic Energy Agency (IAEA), Vienna, Austria, 25–46, 2002.

Lowry, D., Holmes, C. W., Rata, N. D., O'Brien, P., and Nisbet, E. G.: London methane emissions: Use of diurnal changes in concentration and $\delta^{13}C$ to identify urban sources and verify inventories, J. Geophys. Res.-Atmos., 106, 7427–7448, 2001.

Marrero, T. R. and Mason, E. A.: Gaseous diffusion coefficients, J. Phys. Chem. Ref. Data, 1, 3–118, 1972.

Mikaloff Fletcher, S. E., Tans, P. P., Bruhwiler, L. M., Miller, J. B., and Heimann, M.: CH_4 sources estimated from atmospheric observations of CH_4 and its $^{13}C/^{12}C$ isotopic ratios: 1. Inverse modeling of source processes, Global Biogeochem. Cy., 18, GB4004, doi:10.1029/2004GB002223, 2004a.

Mikaloff Fletcher, S. E., Tans, P. P., Bruhwiler, L. M., Miller, J. B., and Heimann, M.: CH_4 sources estimated from atmospheric observations of CH_4 and its $^{13}C/^{12}C$ isotopic ratios: 2. Inverse modeling of CH_4 fluxes from geographical regions, Global Biogeochem. Cy., 18, GB4005, doi:10.1029/2004GB002224, 2004b.

Miller, J. B. and Tans, P. P.: Calculating isotopic fractionation from atmospheric measurements at various scales, Tellus B, 55, 207–214, 2003.

Mischler, J. A., Sowers, T. A., Alley, R. B., Battle, M., McConnell, J. R., Mitchell, L., Popp, T., Sofen, E., and Spencer, M. K.: Carbon and hydrogen isotopic composition of methane over the last 1000 years, Global Biogeochem. Cy., 23, GB4024, doi:10.1029/2009GB003460, 2009.

Myhre, G., Shindell, D., Bréon, F.-M., Collins, W., Fuglestvedt, J., Huang, J., Koch, D., Lamarque, J.-F., Lee, D., Mendoza, B., Nakajima, T., Robock, A., Stephens, G., Takemura, T., and Zhang, H.: Anthropogenic and natural radiative forcing, in: Climate Change 2013: the Physical Science Basis. Contribution of Working Group I to the Fifth Assessment Report of the Intergovernmental Panel on Climate Change, edited by: Stocker, T. F., Qin, D., Plattner, G.-K., Tignor, M., Allen, S. K., Boschung, J., Nauels, A., Xia, Y., Bex, V., and Midgley, P. M., Cambridge University Press, Cambridge, UK, New York, NY, USA, 659–740, 2013.

Nara, H., Tanimoto, H., Tohjima, Y., Mukai, H., Nojiri, Y., Katsumata, K., and Rella, C. W.: Effect of air composition (N_2, O_2, Ar, and H_2O) on CO_2 and CH_4 measurement by wavelength-scanned cavity ring-down spectroscopy: calibration and measurement strategy, Atmos. Meas. Tech., 5, 2689–2701, doi:10.5194/amt-5-2689-2012, 2012.

Pataki, D. E., Ehleringer, J. R., Flanagan, L. B., Yakir, D., Bowling, D. R., Still, C. J., Buchmann, N., Kaplan, J. O., and Berry, J. A.: The application and interpretation of Keeling plots in terrestrial carbon cycle research, Global Biogeochem. Cy., 17, 1022, doi:10.1029/2001GB001850, 2003.

Pétron, G., Frost, G., Miller, B. R., Hirsch, A. I., Montzka, S. A., Karion, A., Trainer, M., Sweeney, C., Andrews, A. E., Miller, L., Kofler, J., Bar-Ilan, A., Dlugokencky, E. J., Patrick, L., Moore Jr., C. T., Ryerson, T. B., Siso, C., Kolodzey, W., Lang, P. M., Conway, T., Novelli, P., Masarie, K., Hall, B., Guenther, D., Kitzis, D., Miller, J., Welsh, D., Wolfe, D., Neff, W., and Tans, P.: Hydrocarbon emissions characterization in the Colorado Front Range: a pilot study, J. Geophys. Res., 117, D04304, doi:10.1029/2011JD016360, 2012.

Pétron, G., Karion, A., Sweeney, C., Miller, B. R., Montzka, S. A., Frost, G. J., Trainer, M., Tans, P., Andrews, A., Kofler, J., Helmig, D., Guenther, D., Dlugokencky, E.,. Lang, P, Newberger, T., Wolter, S., Hall, B., Novelli, P., Brewer, A., Conley, S., Hardesty, M., Banta, R., White, A., Noone, D.,, Wolfe, and Schnell, R.: A new look at methane and nonmethane hydrocarbon emissions from oil and natural gas operations in the Colorado Denver–Julesburg Basin, J. Geophys. Res.-Atmos., 119, 6836–6852, doi:10.1002/2013JD021272, 2014.

Press, W. H., Flannery, B. P., Teukolsky, S. A., and Vetterling, W. T.: Numerical Recipes: the Art of Scientific Computing, Cambridge University Press, Cambridge, 523ff., 1986.

Quantum, G. I. S. Development Team: Quantum GIS Geographic Information System, Open Source Geospatial Foundation, available at: http://www.qgis.org/wiki/Developers_Manual, 2013.

Quay, P. D., King, S. L., Lansdown, J. M., and Wilbur, D. O.: Isotopic composition of methane released from wetlands: implications for the increase in atmospheric methane, Global Biogeochem. Cy., 2, 385–397, 1988.

Rella, C. W., Chen, H., Andrews, A. E., Filges, A., Gerbig, C., Hatakka, J., Karion, A., Miles, N. L., Richardson, S. J., Steinbacher, M., Sweeney, C., Wastine, B., and Zellweger, C.: High accuracy measurements of dry mole fractions of carbon dioxide and methane in humid air, Atmos. Meas. Tech., 6, 837–860, doi:10.5194/amt-6-837-2013, 2013.

Rice, D. D., Fouch, T. D., and Johnson, R. C.: Influence of source rock type, thermal maturity, and migration on composition and distribution of natural gases, in: Hydrocarbon and mineral resources of the Uinta Basin, Utah and Colorado, edited by: Fouch, T. D., Vito F. N., and Chidsey Jr., T. C., Utah Geological Association Guidebook, 20, 95–110, 1992.

Richardson, S. J., Miles, N. L., Davis, K. J., Crosson, E. R., Rella, C. W., and Andrews, A. E.: Field testing of cavity ring-down spectroscopy analyzers measuring carbon dioxide and water vapor, J. Atmos. Ocean. Tech., 29, 397–406, 2012.

Rothman, L. S., Gordon, I. E., Babikov, Y., Barbe, A., Chris Benner, D., Bernath, P. F., Birk, M., Bizzocchi, L., Boudon, V., Brown, L. R., Campargue, A., Chance, K., Cohen, E. A., Coudert, L. H., Devi, V. M., Drouin, B. J.,. Fayt, A, Flaud, J.-M., Gamache, R. R., Harrison, J. J.,. Hartmann, J.-M, Hill, C., Hodges, J. T., Jacquemart, D., Jolly, A., Lamouroux, J., Le Roy, R. J., Li, G., Long, D. A., Lyulin, O. M., Mackie, C. J., Massie, S. T., Mikhailenko, S., Müller, H. S. P., Naumenko, O. V., Nikitin, A. V., Orphal, J., Perevalov, V.,. Perrin, A., Polovtseva, E. R., Richard, C., Smith, M. A. H., Starikova, E., Sung, K., Tashkun, S., Tennyson, J., Toon, G. C., Tyuterev, V. G., and Wagner, G.: The HITRAN2012 molecular spectroscopic database, J. Quant. Spectrosc. Ra., 130, 4–50, 2013.

Schnell, R. C., Oltmans, S. J., Johnson, B. J., and Neely III, R. R.: The Anatomy of Wintertime Photochemical Ozone Production Events in the Upper Green River, WY and Uintah, UT Natural Gas Fields, in: AGU Fall Meeting Abstracts, San Francisco, USA, 3–7 December 2012, Vol. 1, p. 5, 2012.

Schoell, M.: The hydrogen and carbon isotopic composition of methane from natural gases of various origins, Geochim. Cosmochim. Ac., 44, 649–661, doi:10.1016/0016-7037(80)90155-6, 1980.

Simpson, I. J., Andersen, M. P. S., Meinardi, S., Bruhwiler, L., Blake, N. J., Helmig, D., Sherwood Rowland, F., and Blake, D. R.: Long-term decline of global atmospheric ethane concentrations and implications for methane, Nature, 488, 490–494, 2012.

Smith, L. K., Lewis Jr., W. M., Chanton, J. P., Cronin, G., and Hamilton, S. K.: Methane emissions from the Orinoco River floodplain, Venezuela, Biogeochemistry, 51, 113–140, 2000.

Tans, P. P.: US Patent No. 7,597,014, US Patent and Trademark Office, Washington, DC, 2009.

UBETS Report: Final Report: Uintah Basin Energy and Transportation Study, available at: www.utssd.utah.gov/documents/ubetsreport.pdf (last access: 18 June 2014), 2013.

Uintah Map: Uintah County Oil and Gas Wells, created 4/16/2013, available at: http://www.co.uintah.ut.us/gis/Oil%20and%20Gas%20Wells.pdf (last access: 4 July 2014), 2013.

Utah Well Information Query: State of Utah Department of Natural Resources Division of Oil Gas and Mining, Well Information Query, available at: http://oilgas.ogm.utah.gov/Data_Center/LiveData_Search/well_information.htm (last access: February 2013), 2012.

Varghese, P. L. and Hanson, R. K.: Collisional narrowing effects on spectral line shapes measured at high resolution, Appl. Optics, 23, 2376–2385, doi:10.1364/AO.23.002376, 1984.

Werner, R. A. and Brand, W. A.: Referencing strategies and techniques in stable isotope ratio analysis, Rapid Commun. Mass Sp., 15, 501–519, 2001.

White, J. W. C. and Vaughn, B. H.: Stable Isotopic Composition of Atmospheric Methane (^{13}C) from the NOAA ESRL Carbon Cycle Cooperative Global Air Sampling Network, 1998–2014, Version: 2015-08-03, University of Colorado, Institute of Arctic and Alpine Research (INSTAAR), available at: ftp://aftp.cmdl.noaa.gov/data/trace_gases/ch4c13/flask/, last access: 7 September, 2015.

Winderlich, J., Chen, H., Gerbig, C., Seifert, T., Kolle, O., Lavrič, J. V., Kaiser, C., Höfer, A., and Heimann, M.: Continuous low-maintenance $CO_2/CH_4/H_2O$ measurements at the Zotino Tall Tower Observatory (ZOTTO) in Central Siberia, Atmos. Meas. Tech., 3, 1113–1128, doi:10.5194/amt-3-1113-2010, 2010.

Xiao, Y., Logan, J. A., Jacob, D. J., Hudman, R. C., Yantosca, R., and Blake, D. R.: Global budget of ethane and regional constraints on US sources, J. Geophys. Res.-Atmos., 113, D21306, doi:10.1029/2007JD009415, 2008.